A Computational Framework for Capturing and Tracking Failure in Earthen Structures

by

David A. Weed
B.S. (University of Illinois at Chicago) 2006

Thesis submitted in partial fulfillment of the requirements
for the degree of Doctor of Philosophy in Civil Engineering
in the Graduate College of the
University of Illinois at Chicago, 2016

Chicago, Illinois

Defense Committee:
Craig D. Foster, Chair and Advisor
Eduard Karpov
Farhad Ansari
Chien Wu
David Nicholls, Department of Mathematics, Statistics, and Computer Science

To my family,

Kristin, David, Sadie, and Olivia

ACKNOWLEDGMENTS

I learned a great deal about life and science through the process of completing this dissertation. There were many who played a part in this endeavor and thus I would like to take the time to express my gratitude to them here. I would have never made it to this point had I not had the support and tireless love of both my mother, Sandra, and my wife, Kristin. I also dearly thank my children, David Samuel, Sadie Sophie-Pearl, and Olivia Evangeline who, unbeknownst to them, have helped me to stay grounded in reality and expanded my worldview beyond just myself. They have helped me to continue to grow in my humanity throughout this entire process.

I also owe a great debt of gratitude to my advisor, Craig Foster, for taking me on though I was new to finite elements at the time. His teaching paradigm has served as a template and model for what I aspire to be should I venture into a career in academia. I am also indebted to him for introducing me to the world of advanced finite elements and computational techniques. I particularly appreciate the fact that he helped me to prepare presentations for academic conferences and also gave me the opportunity to travel abroad to places like India and China. With the knowledge that he has given me, I am enthused about the prospect of delving further into the world of finite elements, material modeling and computing. All of the experiences I have been afforded through working with Craig have greatly enriched my life in ways that I will reflect on for years to come. I would also like to thank my committee members, Eduard

Karpov, David Nicholls, Farhad Ansari, and Chien Wu. I appreciate their taking the time to read over and review my dissertation.

I would also like to thank Denise Yates and William Walden who both directed and served me and other students under the UIC Bridge to the Doctorate Program. This was invaluable support as he it helped me to complete course work and publish substantive research which served as an encouraging initial start in my career as a scientist. I thank them both for keeping in touch with me even after my tenure in the Bridge to the Doctorate Program ended.

I also thank Ahmed Shabanna for taking me on as a student at the start of my PhD. Being that my undergraduate degree is in bioengineering, he allowed me to pursue a novel topic dealing with the simulation of human knee joint mechanics. From his lab I would like to particularly thank Bassam Hussein, Luis Maqueda, Mike Brown and Graham Sanborn for our research-related discussions and assistance with coding and research writing.

I extend my gratitude to Florencio Diaz for keeping in contact with me throughout my undergraduate and graduate career at UIC. He provided me with support through the Louis-Stokes Alliance Minority and Participation Program (LS-AMP). He was also instrumental in helping me to delve into research in my time as an undergraduate, a decision which led me to pursue research as a graduate student. He also graciously supported me so that I could attend academic conferences, showcase my research, and network with minority faculty and students in the STEM disciplines.

ACKNOWLEDGMENTS (Continued)

In terms of my colleagues in the lab, I am indebted to their support, friendship and many discussions about research and life over the years. Particularly I would like to thank Adam Tennant, Dipika Gongal, Talisa Mohamadenijad, Ahmed El Ghandour, Milad Parvena and Hosein Motamedi. I owe thanks to B.V. Reddy and Gourav K. for providing great depth of insight into earthen materials and structures as well assisting in the procurement of experimental data. I would like to reserve special thanks to both Adam Tennant and Hosein Motamedi. Through our collaboration and vigorous discussions about earthen materials, enhanced finite elements and plasticity I have learned much more than what would have been possible alone. They both have promising and bright futures as academics and scholars. I wish all of my lab members the very best.

I also thank my church community, University Bible Fellowship, which helped me throughout my undergraduate and graduate career in significant ways. They gave me a place of fellowship and introduced me to a group of talented and wonderful people who will be friends for life. I particularly want to thank Benjamin Toh, Jenny and Jim Cook, Charles and Sarah Kim, Joseph Schafer, and David and Sarah Won, and Luis Pena for their support and encouragement.

As for my family members, I thank my father for talking to me about science and computers when I was young, something which undoubtedly piqued my curiosity and led me to study mathematics and engineering. I also thank all of my sisters: Aja, Ashley, Rachael and Mariah. They are wonderful siblings who have always supported me. I also owe a great debt of gratitude to my late grandmother, Lodena Pouncey, who always encouraged me to pursue my education even in difficult circumstances.

ACKNOWLEDGMENTS (Continued)

Lastly, I am thankful to have been supported for several years through the U.S. National Science Foundation Grant, CMMI-1030398. This has given us the time and resources to conduct our computational studies on earthen materials as well as collaborate with our colleagues at IISc.

TABLE OF CONTENTS

TABLE OF CONTENTS (Continued)

CHAPTER **PAGE**

LIST OF TABLES

LIST OF FIGURES

LIST OF FIGURES (Continued)

FIGURE **PAGE**

LIST OF FIGURES (Continued)

FIGURE **PAGE**

LIST OF FIGURES (Continued)

FIGURE **PAGE**

LIST OF FIGURES (Continued)

FIGURE **PAGE**

LIST OF FIGURES (Continued)

FIGURE **PAGE**

SUMMARY

Within a finite element context, the embedded strong discontinuity approach for strain localization has been used extensively to model localized deformation and fracture in geomaterials. As a fracture propagates, any changes in orientation will inhibit sliding and force the surfaces, in some locations, to open. Some previous models feature only a single sliding degree of freedom. As the surfaces slip in such models, an artificial hardening occurs, creating a geometric locking effect. To this end, we implement a formulation, which, in addition to sliding, possesses an opening degree of freedom. We develop a traction-separation model that allows for coupled opening and shearing displacement in tension, as well as frictional sliding in compression. This thesis compares the single degree of freedom formulation with the model containing both degrees of freedom. We show that the locking effect is alleviated. In addition, a combined implicit-explicit integration scheme for increasing the robustness of softening problems is featured.

Additionally, a new method for embedding predefined interfaces within an arbitrary finite element mesh is proposed and demonstrated. The algorithm for generating these predefined surfaces is detailed and subsequently applied to masonry structures composed of earthen materials to demonstrate its efficacy. Within a given finite element, the initiation of fracture or slippage may occur simultaneously along a predefined interface and in the bulk of the element. In order to determine which surface is critical, we feature a criteria which aids in determining the correct surface upon which all further slippage due to fracture will occur. This interface

method is cast in the framework of an enhanced strain finite element which is capable of capturing softening along an embedded strong discontinuity [1, 2].

The aforementioned methods comprise a framework for simulating fracture problems in earthen structures and materials. The end goal is to gain further insight into their various failure mechanisms.

CHAPTER 1

INTRODUCTION

1.1 Background and motivation

In our present day, as global awareness about energy conservation and the reduction of environmental waste and pollution is steadily growing, some are seeking to borrow from and adopt building techniques which are currently being used in developing nations. About a third of the world uses some type of earthen-based material to construct buildings. These structural materials possess several attractive characteristics such as low embodied energy, high thermal mass, low cost, local availability of materials, and recyclability. The earthen materials which are a focus of this study are commonly composed of sand, gravel, clay and a minimal amount of cement. Bricks intended for masonry usage composed of these materials are usually manufactured with the use of a mechanical press. Remarkably, the strength of earthen bricks is comparable to that of some fired brick. The mortar is of a similar composition and, in contrast to traditional masonry practices in the West, it may be of comparable or higher strength than that of the brick. The differing Poissons' ratio of the materials may also significantly affect the overall strength of the masonry constructed from these materials. Reddy and coworkers shed light on this [3] revealing that the Poissons' ratio of the brick and mortar will significantly affect the lateral stresses experienced and overall compressive strength in a given masonry unit. Some

other studies which have investigated the properties and performance of these earthen blocks can be found in these relevant publications [4–11]

In addition to earthen blocks, structures made from rammed earth are also viable habitation structures. Rammed earth is similar in composition to earthen bricks, however the compaction process occurs on a physically larger scale and with the use of forms. Again, structures made from these materials are ubiquitous in developing nations and have been studied extensively from an experimental standpoint [12–17].

Masonry structures, under in-plane loading, exhibit failure mechanisms such as mortar joint slippage, brick cracking and mortar joint splitting, and spalling within the middle plane [18]. Given these complex interactions, the finite element method (FEM) can aid in understanding these materials' mechanics on a fundamental level. Indeed, FEM has been used in a number of innovative ways to study masonry structures. The doctoral thesis of Rots [19] focused on the computational modeling of concrete fracture. This publication utilized the concept of the strong discontinuity to model material failure within a finite element framework. He also developed an interface model to take into account debonding and failure of composite material joints. Rots later collaborated with Lourenco [20] and extended the interface concept, coupling it with an inelastic constitutive model able to capture deformation and failure in masonry joints. Before this, Lotfi and Shing [21] developed a novel constitutive model based on energy considerations which captured inelastic material behavior of masonry within a finite element framework. They collaborated again in 1994 to focus on an interface model to simulate the effects of masonry joint

deformation. After this, a number of constitutive models focused on the interface technology due to the critical nature of the joints [22–24].

A technique which has shown promise is homogenization ([25, 26]), which aims to solve macroscopic masonry problems in two stages: first a micro-mechanics problems is solved for the material constituents and second, the macroscopic masonry problem is solved using a finite element approach. Similarly, a multiscale damage model approach is featured by Massart and coworkers [27]. Sacco [28] utilized homogenization and extended this work with Marfia [29] to formulate a multiscale damage friction model to solve problems which featured periodic masonry.

Another approach has been to focus structures which feature mortar that is much weaker in strength than the brick and thus relegate their failure analysis exclusively to the brick-mortar joints. Chaimoon and Attard [30] have investigated the behavior of unreinforced masonry walls under shear and compressive loads using a formulation that focuses on inelasticity and failure at the masonry joints. Additionally, they have applied their model to investigate masonry under three-point bending loads. Reyes and coworkers have applied a cohesive zone model with the use of embedded discontinuities to investigate the behavior of brick-masonry under various loading conditions [31, 32]. Radulovic and Mosler used a similar embedded approach and extended their study to three dimensional formulations [33]. Using a mesoscale approach, Vandoreen and coworkers have compared the effects of using either weak discontinuities or strong discontinuities in modeling the brick-mortar interfaces [34]. More recently, Minaie and

coworkers [35] incorporated non-linear finite element analysis in their study of the response of reinforced shear walls under bi-directional loading.

However, for earthen structural materials, the literature is somewhat sparse. Though there is, nonetheless, a growing body of research investigating the behavior of both earthen blocks and rammed earth. Notably, Vyas and Reddy [36] employed FEM in order to predict the compressive strength of solid block masonry. Akbarzade and Tasnimi investigated the inelastic behavior of masonry built from materials similar to compressed earth blocks [37]. Srisanthi and coworkers utilized a three-dimensional model in order to study earthquake effects on masonry comprised of earthen blocks [38]. In recent years, a number of studies have investigated the behavior of rammed earth using FEM [39–42].

1.2 Enhanced Finite Element Formulation for Failure

Material softening is a complex phenomenon that has been approached in a number of ways over the years, from both a continuum mechanics and computational standpoint. The strategy taken in this study, which builds upon [43] and [44], is predicated upon the detection of narrow bands of localized strain. With a focus on finite element implementation of localization theory, Simo and coworkers [1] coupled the Assumed Enhanced Strain (AES) method with the Strong Discontinuity Approach (SDA) to solve boundary value problems which focused on capturing material softening. Oliver and coworkers developed a formulation which sought to make a smooth transition from intact continuum to damaged material [45]. In a comparative study, Jirasek categorized several general formulations of the embedded discontinuity method.

Later, he and Belytschko compared the aforementioned method with the extended finite element method (XFEM). Extended and Generalized Finite Elements have received significant in modeling fracture [46–51]. The observation was that though the embedded method suffered from robustness issues (which would later find remedy in [52]) it remained an attractive choice due to the fact that the nodes arising from a discontinuity band can be condensed out on the element level. This is a contrast to XFEM which introduces extra nodal degrees of freedom to the global stiffness matrix. Since this field possesses such an adequate base of knowledge, the SDA coupled with AES method is chosen model the softening behavior of the masonry materials featured in this study. This thesis closely follows the particular embedded discontinuity formulation found in [53–58].

1.3 Constitutive model for capturing fracture

A vast array of techniques suited for capturing localized material softening has been proposed in the literature. Various formulations arising from the cohesive zone model (CZM) methodology have been a popular choice for some time. This method was developed to resolve the prevalence of singularities that arise in linear elastic fracture mechanics theory. Additionally, the method is able to model non-linear behavior, which is inherent in fracture-based problems. Initial work in this area was undertaken by Dugdale [59], who devised a cohesive zone formulation to model brittle materials. Shortly after Barenblatt [60] applied similar concepts to capturing inelastic deformation as well as the onset of yielding at crack tips. Later, many novel innovations, used to solve a wide range of failure and fracture-related problems, followed as summarized

and remarked upon in [61]. The model used in this thesis was developed by the author and coworkers in [62]. It focuses on capturing fracture in two regimes, compression and tension. For a discontinuity surface in tension, the normal and tensile tractions are governed by an elliptical interaction which is augmented by a parameter that takes into account the energy release rate of the material. In compression, a Mohr-Coulomb approach is taken in that the shear traction is balanced against the force of friction and cohesion. This model is suited for geomaterials which may experience intense shear deformation as well as tensile effects.

1.4 Predefined Interfaces

An integral part of studying masonry structures is the incorporation of interface technology which can accurately capture the various effects of masonry joints on the macroscopic assemblage. Allix and Corigliano [63] introduced a computational model and scheme for simulating debonding and damage between the interfaces of composite materials. Mroz and Giambanco [64] developed an interface constitutive model which takes into account effects due to asperities between surfaces as well as dilatancy within joints, including rock and masonry joints. Alfano and Crisfield, starting with delamination problems [24], eventually extended this work with interface elements, with the addition of a friction formulation, to masonry as well [65]. Camanho used a three-dimensional formulation which featured zero-width interface volume elements to study delamination in composites [66, 67]. In more recent work, De Lorenzis [68] investigated the affects of interfaces on the structural integrity of composite materials, particularly macroscopic characteristics such as strength, ductility and stiffness. This found applications in masonry

arches and debonding between fiber reinforced laminates. Shieh-Beygi and Pietruszczak [69] note that past masonry modeling approaches, which featured continuum elements in the masonry units and interface elements in the masonry joints, were deficient in that they could not accurately capture the interaction of the various masonry constituents.

The interface model presented in this thesis features predefined weak planes as masonry joints, these interfaces are embedded within bulk elements which are susceptible to inelastic effects as well as damage. This interface technology is based off of the work of Foster and coworkers [57], who presented preliminary examples utilizing interfaces by way of a novel edge-finding algorithm. These interfaces are treated as embedded discontinuities and thus their degrees of freedom can be condensed out of the global stiffness matrix, thereby increasing computational efficiency. They are also given their own unique materials properties such as friction angle, cohesion, characteristic slip length as well as a parameter based on the energy release rate of the material in question.

1.5 Structure of this dissertation

The remainder of this dissertation is structured as follows: Chapter 2 details the kinematics of strong discontinuities and briefly explains the method for ascertaining the inception and orientation of a given failure surface. Additionally, the post-localization constitutive model is explained in detail. This chapter also features a modified version of the method found in [52] which was developed to enhance the robustness of boundary value problems modeled with the embedded discontinuity method. Lastly, examples which showcase the post localization

constitutive model are shown and compared against a previous formulation which featured on a sliding degree of freedom.

Chapter 3 focuses on the interface technology used to model material preexisting weak planes in structural assemblages. We detail the algorithm which is used to propagate these interfaces as well as the yield criteria and subsequent constitutive model used once a surface is activated. This is followed by examples of periodic-structured masonry assemblages which show diffuse failure through the brick or bulk as well as along the interfaces.

Chapter 4 showcases the application of the traction-separation model, preexisting interface technology, and a plasticity model suited for geomaterials to a simulation involving a laterally loaded rammed earth structure.

Chapter 5 details the conclusions drawn from this work and discusses relevant topics to explore in the future.

CHAPTER 2

A COMBINED OPENING-SLIDING FORMULATION FOR USE IN MODELING GEOMATERIAL DEFORMATION AND FRACTURE PATTERNS

2.1 Introduction

The numerical modeling of geomaterials, particularly in the context of finite element analysis, has a wide and varied base of research behind it. As part of these developments over the past two decades, embedded discontinuities have been investigated for use in numerical models which seek to capture failure due to localized softening. The concept of a so-called weak discontinuity was developed in order to capture narrow shear bands of deformation within materials [70, 71]. Shear bands were first described in metals by Tresca [72]. Later, this nomenclature was adopted by the geomechanics community in order to describe similar phenomenon seen in soil and rock-like materials. Subsequently, numerical models were developed in order to replicate this behavior in simulations. Precipitated from this line of research was the strong discontinuity approximation. When the width of the discontinuity is small compared to that of the overall structure the weak discontinuity may be simplified by reducing it to zero width. Simo and co-workers showed in seminal reports [1, 73] that the post-localization softening modulus of the material as well as the plastic multiplier necessarily take on a distributional representation. In

addition to this representation, they introduced a re-parametrized displacement and strain field which is suited for capturing both measures of deformation within a finite element context.

The model presented in this chapter is an extension of the Mohr-Coulomb slip model for geological materials in [53, 54, 56, 57, 74]. The main contribution of this chapter is the introduction of a post-localization constitutive model allowing for slip in directions both tangential and normal to a given discontinuity band. The impetus for this is two-fold. In reality, as geomaterials begin to localize and subsequently fail in either the compressive or tensile regime, material may not only slide but also, noticeable movement in the direction normal to the failure surface is observed. Even for far-field compression, the development of a model which takes into account the interaction of both compressive and tensile traction is in order.

Carol et al. [75] developed a hyperbolic yield surface in order to capture the effect of tension and a linear one for the purely compressive regime. This model was later adopted by Galvez, et al. [**?**] for the purposes of simulating material failure in masonry structures. The model in this chapter is similar to that of Carol and Galvez in that it captures the aforementioned deformation regimes. Camacho and Ortiz [76] developed a model which features an elliptical interaction between the shear and normal tractions on a given deformation band. In this model, a material parameter is employed to control the contribution of the shear traction on the surface, a feature which is later used in [77]. In a similar a vein, we develop a model which features elliptical interactions between both the tractions and displacements (normal and tangential to the surface cf. [78]), based on the material's strain energy release rate.

Secondly, in [57] simulations yielded results which revealed that a model only incorporating a single, sliding degree of freedom gave rise to geometric locking which was mesh-dependent. Specifically, this effect arose due to the model's inability to accurately capture opening displacements. From this observation, the conjecture was that remedies such as rotating or extra degrees of freedom [2, 79] would alleviate geometric locking. The authors in this chapter took the latter approach by developing a constitutive model which features both opening and sliding degrees of freedom on the discontinuity surface. When the band is in compression, it is only subject to deformation tangential to its surface. Hence, friction and cohesion forces impede sliding on the localization band. However, when tension is present the band experiences a combination of opening normal to the surface in addition to the aforementioned tangential sliding, albeit without friction. We show that such a model presents a more realistic depiction of the mechanics of softening behavior within soil-based materials. Through several benchmark examples, this chapter shows that the currently proposed constitutive model alleviates the spurious geometric locking effect seen in [57].

In this particular study, we focus on a damage-like formulation which assumes elastic unloading toward the origin in the spirit of (localized) damage mechanics, and the tradition of cohesive zone formulations. For simplicity, we will consider a constant friction coefficient. However, this is not a requirement. By ramping up the friction coefficient as the cohesion degrades, we can recreate the simplified slip weakening formulation as described in Borja and Foster [56]. Variable friction as detailed in [80] and [57] can also be implemented.

Softening problems within the strong discontinuity framework are well known to have robustness and stability issues [81**?** , 82]. To this end, we incorporate a combined implicit-explicit integration method (Impl-Ex), modified from a scheme devised by Oliver and co-workers [52], which renders the local stiffness matrices associated with softened elements positive definite. We show that this allows problems with complex geometries to converge, whereas using a fully implicit integration scheme does not.

The remainder of the chapter is structured as follows: Section 2 gives a general overview of strong discontinuity kinematics in the context of small strain. Additionally, in this section, the localization criterion, which indicates the onset of the formation of a strong discontinuity, is given a brief review. Section 3 briefly discusses some fundamental aspects of an enhanced strain finite element. The constitutive model for slip weakening within a localized element is described in Section 4. The numerical implementation of the model is given in Section 5. Section 6 shows the derivation of the stiffness formulation. Numerical examples and closing remarks conclude the chapter.

2.2 Kinematics

2.2.1 Continuum Equations

Here we describe the kinematical relationship between continuous and discontinuous displacements within an arbitrary continuously smooth volume (Figure 1). Note that for the purposes of this study, our analysis is relegated to the realm of infinitesimal strains. The continuous displacements are distributed throughout the volume while the discontinuous displacements are

contained on the discontinuity surface S. The total displacement field in the body is given by the form:

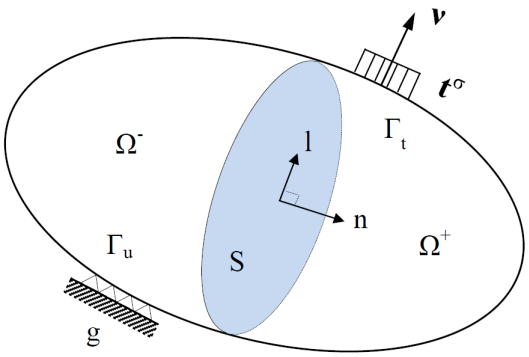

Figure 1: Arbitrary volume with embedded strong discontinuity surface

$$\boldsymbol{u} := \bar{\boldsymbol{u}} + [\![\boldsymbol{u}]\!] H_S(\boldsymbol{x}) \tag{2.2.1}$$

where $\bar{\boldsymbol{u}}$ is the vector of continuous displacements and $[\![\boldsymbol{u}]\!]$ designates the vector of displacements along the strong discontinuity. This vector takes the form:

$$[\![\boldsymbol{u}]\!] = \boldsymbol{\zeta} = \zeta_s \boldsymbol{l} + \zeta_n \boldsymbol{n} \tag{2.2.2}$$

Where $\boldsymbol{l}$ and $\boldsymbol{n}$ are unit vectors which are tangential and normal to the discontinuity surface, respectively.

$H_S(\boldsymbol{x})$ is the standard Heaviside function across the discontinuity surface S defined by the conditions

$$H_S(\boldsymbol{x}) = \begin{cases} 1 & \texttt{if} \quad \boldsymbol{x} \in \Omega^+ \\ 0 & \texttt{if} \quad \boldsymbol{x} \in \Omega^- \end{cases} \tag{2.2.3}$$

The strain tensor is found by taking the symmetric part of the gradient of the displacement vector:

$$\boldsymbol{\epsilon} := \nabla^s \boldsymbol{u} = \nabla^s \bar{\boldsymbol{u}} + \nabla^s \left[\!\left[\boldsymbol{u}\right]\!\right] H_S + \left(\left[\!\left[\boldsymbol{u}\right]\!\right] \otimes \boldsymbol{n}\right)^s \delta_S \tag{2.2.4}$$

where $\nabla H_S = \boldsymbol{n}\delta_S$. The physical meaning of the last term is that the strain is unbounded on the discontinuity surface S.

For the purposes of this study, the jump magnitude is considered to be spatially invariant (piece-wise continuous across the elements). Thus the second term is omitted from the equation, leaving the final form of

$$\boldsymbol{\epsilon} := \nabla^s \boldsymbol{u} = \nabla^s \bar{\boldsymbol{u}} + (\llbracket \boldsymbol{u} \rrbracket \otimes \boldsymbol{n})^s \, \delta_S \tag{2.2.5}$$

2.2.2 Localization Condition

In this section, the procedure that is used to detect the onset of strain localization is outlined. Hill [83] investigated the physics of wave propagation in solids in order to determine the onset of inelastic behavior therein. Rudnicki and Rice, in [84], built off of this work introducing a mathematical framework for detecting shear band localization. Since then, bifurcation theory has been widely used to determine the onset of softening behavior of various geomaterials.

To begin, we posit that at any given time, the traction rate along the discontinuity surface must be continuous. Using a general non-associative plasticity model, i.e., where F is an arbitrary yield function and G is a plastic potential, the traction rate is written as

$$\dot{\boldsymbol{t}} = \dot{\boldsymbol{\sigma}} \cdot \boldsymbol{n} = \boldsymbol{n} \cdot \boldsymbol{c}^e : \left(\dot{\boldsymbol{\epsilon}} - \dot{\lambda} \frac{\partial G}{\partial \boldsymbol{\sigma}} \right) \tag{2.2.6}$$

Where $\boldsymbol{c}^e$ is the elastic modulus tensor and $\dot{\lambda}$ is the rate of the plastic multiplier.

From [55] $\dot{\lambda} = \dot{\lambda_\delta} \delta_S$

where $\dot{\lambda_\delta} = \frac{1}{\chi}\frac{\partial G}{\partial \boldsymbol{\sigma}} : \boldsymbol{c}^e : (\llbracket \dot{\boldsymbol{u}} \rrbracket \otimes \boldsymbol{n})^S$ and $\chi = \frac{\partial F}{\partial \boldsymbol{\sigma}} : \boldsymbol{c}^e : \frac{\partial G}{\partial \boldsymbol{\sigma}}$

Substituting this into (2.7) yields

$$\dot{\boldsymbol{t}} = \underbrace{\boldsymbol{n} \cdot \boldsymbol{c}^e : \nabla^S \dot{\boldsymbol{u}}}_{\dot{\boldsymbol{t}}} + \underbrace{\boldsymbol{c}^{ep} : (\llbracket \dot{\boldsymbol{u}} \rrbracket \otimes \boldsymbol{n})^S}_{\dot{\boldsymbol{t}_\delta}} \delta_S \tag{2.2.7}$$

where the term $\boldsymbol{c}^{ep} = \boldsymbol{c}^e - \frac{1}{\chi}\boldsymbol{c}^e : \frac{\partial G}{\partial \boldsymbol{\sigma}} \otimes \frac{\partial F}{\partial \boldsymbol{\sigma}} : \boldsymbol{c}^e$ is the elastic-perfectly plastic tangent modulus.

In order for the traction to be bounded, the discontinuous part must vanish, hence

$$\dot{\boldsymbol{t}_\delta} = \boldsymbol{n} \cdot \boldsymbol{c}^{ep} : (\llbracket \dot{\boldsymbol{u}} \rrbracket \otimes \boldsymbol{n})^s = \boldsymbol{0}$$

Noting that $\llbracket \dot{\boldsymbol{u}} \rrbracket = \dot{\zeta}\boldsymbol{m}$, this expression can be re-written as

$$(\boldsymbol{n} \cdot \boldsymbol{c}^{ep} \cdot \boldsymbol{n}) \cdot \boldsymbol{m} = \boldsymbol{A} \cdot \boldsymbol{m} = \boldsymbol{0} \tag{2.2.8}$$

where $\boldsymbol{m}$ is the slip direction on the discontinuity surface and $\boldsymbol{A}$ is the elastic-perfectly plastic acoustic tensor.

This quantity is zero only when $\boldsymbol{A}$ becomes singular, that is, when $\det(\boldsymbol{A}) = 0$.

Eq. **??** can be solved iteratively, as detailed in [43] and [85], in order to determine the direction of the jump, $\boldsymbol{m}$, along the discontinuity.

2.3 Finite Element Implementation

2.3.1 Re-parameterization of displacement field

Here, we use the parametrized form of the displacement introduced by Simo and co-workers [1]. Within a standard Assumed Enhanced Strain (AES) framework, the displacement field is re-cast such that the continuous part conforms to the standard finite element formulation and the discontinuous part is considered as an additional enhancement to the displacement field. Hence,

$$\boldsymbol{u}^h = \boldsymbol{u}^{h,conf} + \boldsymbol{u}^{h,enh} \tag{2.3.1a}$$

$$\boldsymbol{u}^h = \hat{\boldsymbol{u}}^h + \left[\!\left[\boldsymbol{u}^h\right]\!\right] M_S^h\left(\boldsymbol{x}\right) \tag{2.3.1b}$$

where $M_S^h\left(\boldsymbol{x}\right) = H_S - f^h$. Hence,

$$\boldsymbol{u}^h = \left(\bar{\boldsymbol{u}}^h + \left[\!\left[\boldsymbol{u}^h\right]\!\right] f^h\right) + \left[\!\left[\boldsymbol{u}^h\right]\!\right]\left(H_S - f^h\right) \tag{2.3.1c}$$

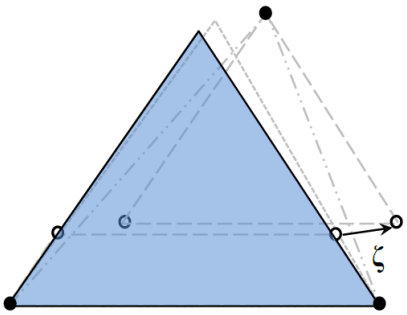

Figure 2: An undeformed CST element.

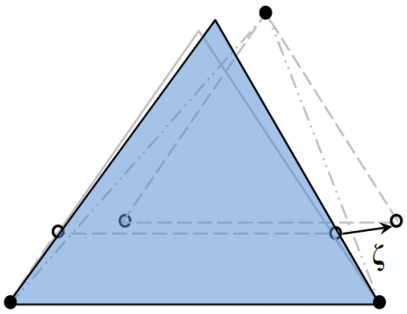

Figure 3: The previously undeformed element which has now undergone an arbitrary displacement ($\bar{\boldsymbol{u}}$).

The term, f^h, is an arbitrary smooth function which, on a given element with a discontinuity, meets the criteria

$$f^h = \begin{cases} 1 & \texttt{if} \quad e_n \in \Omega^+ \\ \\ 0 & \texttt{if} \quad e_n \in \Omega^- \end{cases} \tag{2.3.2}$$

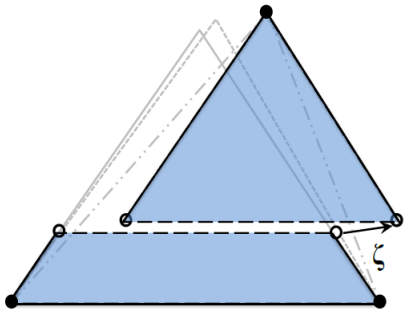

Figure 4: The total displacement within the element after experiencing a displacement jump ($\boldsymbol{u}$)

.

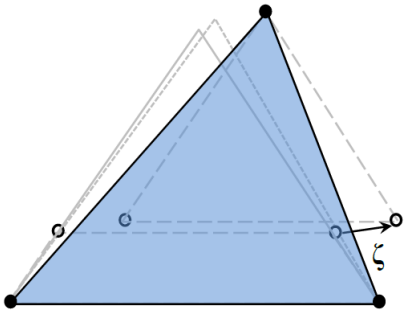

Figure 5: Using the re-parametrization technique, the final 'conforming' displacement of the element ($\hat{\boldsymbol{u}}$)

.

and e_n is the element node number. For this study, f^h takes the particular form of

$$f^h = \sum_{A=1}^{n_{en}} N_A H_S(\boldsymbol{x}_A) \tag{2.3.3}$$

where n_{en} is the set of active nodes within a given element, i.e. nodes that are in Ω^+. For each element, the conforming displacement field is composed of the continuous nodal displacements as well as the contribution of the displacements along the localization band. This part of the displacement "conforms" to the standard finite element shape functions, hence

$$\boldsymbol{u}^{h,conf} = \sum_{A=1}^{n_{en}} N_A \boldsymbol{d}_A \tag{2.3.4}$$

The strain tensor is obtained by taking the symmetric part of the gradient of the displacement in Equation 2.3.1c yielding,

$$\begin{aligned} \boldsymbol{\epsilon}^h &= \boldsymbol{B}\boldsymbol{d} + \left[(\boldsymbol{\zeta} \otimes \boldsymbol{n})^s \, \delta_S - \left(\boldsymbol{\zeta} \otimes \nabla f^h \right)^s \right] \\ &= \boldsymbol{\epsilon}^{h,conf} + \boldsymbol{\epsilon}^{h,enh}. \end{aligned} \tag{2.3.5}$$

In terms of recovering the finite element stress, it is convenient to denote the strain in terms of a regular or continuous part and a singular or jump part:

$$\boldsymbol{\epsilon}^h = \underbrace{\boldsymbol{B}\boldsymbol{d} - \left(\boldsymbol{\zeta} \otimes \nabla f^h \right)^s}_{regular} + \underbrace{(\boldsymbol{\zeta} \otimes \boldsymbol{n})^s \, \delta_S}_{singular} \tag{2.3.6}$$

as shown in [55], the finite element stress for localized elements is derived from the regular part of the strain, hence

$$\dot{\boldsymbol{\sigma}}^h = \boldsymbol{c}^e : \dot{\boldsymbol{\epsilon}}^{h,reg} \tag{2.3.7}$$

2.4 Post-localization Constitutive Model

2.4.1 Yield Criteria

Once localization has been detected and the orientation of the critical surface determined, the mechanics of the softening behavior on the surface must be defined. There are several ways to approach this model. Oliver [86] has shown that the continuum model can be used to induce a localized model. The great advantages of this approach are that a smooth and consistent transition from continuum to localized response is assured, and the material response is consistent with experimental data. However, it may also be argued that the mechanics of the localized material differ from the bulk continuum response since this is a separate mechanism. In this case, a separate constitutive model must be introduced for the localized behavior. The form of that model is the subject of this section.

The initial cohesion on the surface is determined to be consistent with the stress state at localization. The yield strength in pure tension may be different, and thus is assumed to differ by a constant factor of α_σ. The constant, α_σ can be thought of as the reciprocal of the parameter β, which is described as a shear stress factor in Camacho and Ortiz [76]. Similarly,

Alfaiate et al. [87] uses a parameter which controls the contribution of the shear jump on the deformation band. These parameters were likely motivated by the nature of the boundary value problems (BVP) that were being solved, namely fractures within brittle materials under tension. Though mixed-mode behavior is observed in experiments where tensile forces are present, eventually Mode I or opening fractures often dominate the deformation and subsequent fracture of the material. Therefore, in order to fit experimental data well, it is prudent to control the contribution of the shear traction or displacement present within the fracture zone. In contrast, for geomaterials, normal stresses are usually, thought not always, compressive and shear localization under compression is often observed. For BVPs of this nature, controlling the normal traction contribution may aid in accurately fitting experimental data.

The yield function that we incorporate takes two forms. When compressive normal traction is present on the band, the yield function takes the form of a Mohr-Coulomb law (Equation 2.4.1). In the case of tensile normal traction, the interaction between the shear and normal traction is assumed to be elliptical (Equation 2.4.2).

$$\Phi_{\text{compression}} = 0 = |\tau - c \cdot \text{sign}(\zeta_s)| - f \tag{2.4.1}$$

$$\Phi_{\text{tension}} = 0 = \sqrt{(\tau)^2 + (\alpha_\sigma \langle\sigma\rangle)^2} - c \tag{2.4.2}$$

where $\sigma = \boldsymbol{n} \cdot \boldsymbol{\sigma} \cdot \boldsymbol{n}$ is the normal traction, $\tau = \boldsymbol{l} \cdot \boldsymbol{\sigma} \cdot \boldsymbol{n}$ the shear traction on the deformation band. ζ_s is the amount of slip in the direction parallel to the deformation band and c is the cohesion. $\langle \cdot \rangle$ are the Macaulay brackets $[\langle x \rangle = (x + |x|)/2]$, signifying the positive part of the quantity. Hence in compression, the normal traction only influences the yield function in the frictional traction $f = \mu \langle -\sigma \rangle$. For this study, we use a static coefficient of friction, though a variable coefficient, as in [56, 57], can be used.

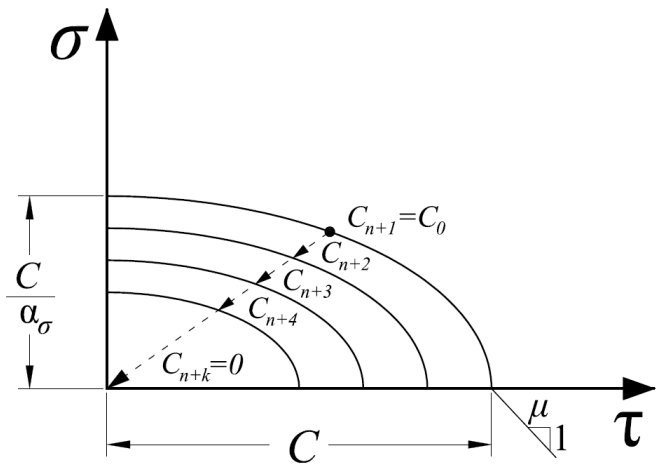

Figure 6: Normal and shear traction interaction on yield surface

2.4.2 Tensile Regime

In tension, the friction force is absent, therefore according to Eq. Equation 2.4.2 the equivalent stress on the band is

$$\sigma_{eq} = c = \sqrt{\tau^2 + (\alpha_\sigma \sigma)^2} \tag{2.4.3}$$

We relate the stiffness parameter, k_s, to the traction on the band

$$\begin{aligned} \sqrt{\tau^2 + (\alpha_\sigma \sigma)^2} &= c \\ \vdots \quad &= c_0 \left(1 - \frac{\zeta_{eq}}{\zeta^*}\right) \\ \vdots \quad &= c_0 \left(1 - \frac{\zeta_{eq}}{\zeta^*}\right) \frac{\zeta_{eq}}{\zeta_{eq}} \\ \vdots \quad &= c_0 \left(\frac{1}{\zeta_{eq}} - \frac{1}{\zeta^*}\right) \zeta_{eq} \\ \sigma_{eq} \quad &= k_s \zeta_{eq} \end{aligned} \tag{2.4.4}$$

where $\zeta_{eq} = \sqrt{{\zeta_s}^2 + (\alpha_\zeta \zeta_n)^2}$. The material parameter, α_ζ, signifies the differing weights of the opening and shear displacements.

We now postulate two balance laws which relate the tractions and displacements both normal and tangential to the deformation band:

$$\alpha_\sigma \sigma = k_s \alpha_\zeta \zeta_n \tag{2.4.5}$$

$$\tau = k_s \zeta_s. \tag{2.4.6}$$

Eq. Equation 2.4.5 can also be written as

$$\begin{aligned} \sigma &= \frac{\alpha_\zeta}{\alpha_\sigma} k_s \zeta_n \\ &= k_n \zeta_n \end{aligned} \tag{2.4.7}$$

where k_n represents the stiffness in the direction of the normal traction on the band. If we rewrite this stiffness parameter, solving for α_σ, we have $\alpha_\sigma = \frac{\alpha_\zeta}{k_n} k_s$. This is substituted into Eq. Equation 2.4.3 giving

$$\sigma_{eq} = \sqrt{\tau^2 + \left(\frac{\alpha_\zeta k_s}{k_n}\sigma\right)^2}.$$

Further, substituting the forms in the traction-displacement balance laws in Eqs. Equation 2.4.5 and Equation 2.4.6 yields

$$\begin{aligned} \sigma_{eq} &= \sqrt{(k_s \zeta_s)^2 + (\alpha_\zeta k_s \zeta_n)^2} \\ &= k_s \sqrt{\zeta_s^2 + (\alpha_\zeta \zeta_n)^2} \\ &= k_s \zeta_{eq} \end{aligned}$$

which recovers Eq. Equation 2.4.4, verifying the coupled nature of the tractions and displacements on the deformation band.

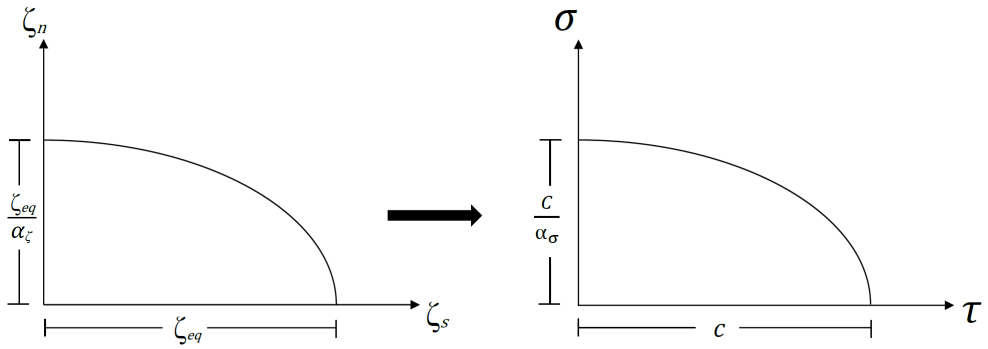

Figure 7: For a deformation band experiencing tension, the slip degrees of freedom are coupled with the tractions.

2.4.2.1 Determining the parameters α_σ and α_ζ

These parameters are related to one another vis à vis the fracture energy in each of the respective fracture modes. The specific fracture energy for Mode I (opening) and Mode II (sliding) (Figure 8) is simply the area under the respective curves (cf. [88]). Therefore

$$G_I = \frac{1}{2}\frac{\zeta^*}{\alpha_\zeta}\frac{c}{\alpha_\sigma} \tag{2.4.8}$$

$$G_{II} = \frac{1}{2}\zeta^* c \tag{2.4.9}$$

The fracture energy is related to the stress intensity factor, K, through the equation

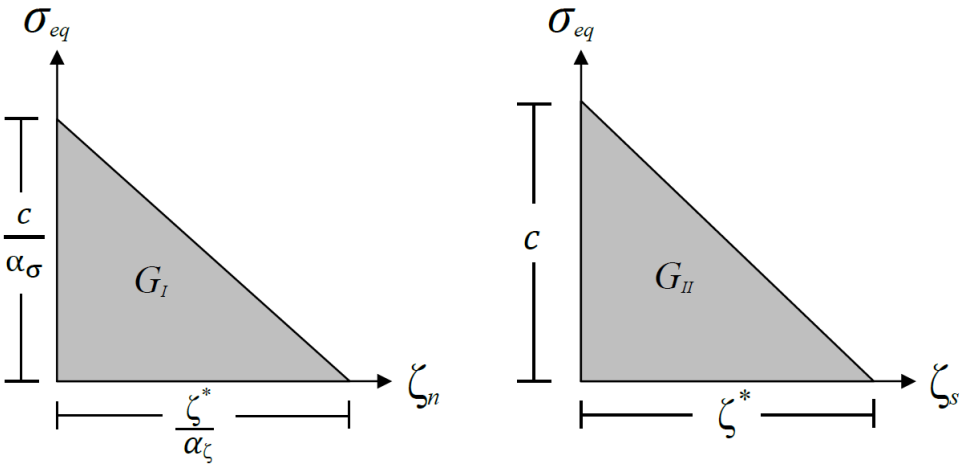

Figure 8: The fracture energy for opening and sliding fractures

$$G = \frac{K^2}{E}(1-\nu^2) \tag{2.4.10}$$

which is valid for plane strain.

Hence, the ratio of the corresponding stress intensity factors is

$$\left(\frac{K_{II}}{K_I}\right)^2 = \frac{G_{II}}{G_I} = \alpha_\zeta \cdot \alpha_\sigma \tag{2.4.11}$$

There are many solutions to Eq. Equation 2.4.11, however in this study, we choose the solutions in which $\alpha_\zeta = \alpha_\sigma$. In [89], the empirical value for the ratio $\frac{K_{II}}{K_I}$ varies between 1.13, which corresponds to softer marble, and 2.19, for limestone. In this study, we simply choose $\alpha_\zeta = \alpha_\sigma \approx 2.0$. In a future study that will feature the combination of this model and the plasticity model detailed in [90], we choose a value closer to that of limestone (which is ≈ 2.14), for that will be the particular material of interest. It is worth noting that authors in [76] derived $\alpha_\zeta = 1/\alpha_\sigma$ on energy considerations. However, this creates equal fracture energy in Mode I and II, which is not observed in many materials.

2.4.3 Compressive Formulation

The cohesive formulation is exactly the same as in the tensile case. However, the normal effects on σ_{eq} are neglected. In other words, under compression $\sigma_{eq} = \tau$. In addition to this, the normal displacement on the band is assumed to be zero. Hence, $\tau = k_s \zeta_s$.

However, in addition to cohesive tractions, there is a friction force, defined earlier as $f = \mu \langle -\sigma \rangle$. Under compression, the frictional force acts independently of the displacement, and hence is always active. The final form of the traction balance in this case may be written as

$$|\tau - k_s \zeta_s| \leq f \tag{2.4.12}$$

where strictly less than implies no motion on the band, and equality allows for slip.

For many quasi-brittle materials, there is actually noticeable dilation along shear bands and fracture interfaces due to the mismatch of rough surfaces, wear, and the resulting gouge material [91]. However, this often small and is beyond the current scope of this work.

2.4.4 Cohesion Softening Formulation

The cohesive formulation we will use takes the form of a traction-displacement relationship, common in the cohesive zone formulations such as [76, 92**?**]. This formulation follows the spirit of localized damage mechanics, so that the interface softens with increased displacement, but unloads elastically. Reloading is also elastic until the previous displacement level is reached, where damage continues (Figure 9). For our particular formulation, we use a linear form given by the equation

$$c = c_0 \left(1 - \frac{\zeta_{eq}}{\zeta^*}\right) \tag{2.4.13}$$

where c is exactly the cohesion along the surface in standard Mohr-Coulomb criteria, c_0 is the initial cohesion at the time of localization, ζ_{eq} is the scalar value of the magnitude of the slip on the band and ζ^* is the slip distance until the cohesion completely degrades to zero.

In the literature, several other cohesion softening laws, particularly suited for brittle materials such as concrete, are bilinear [93, 94], exponential [95, 96], and power-law based [97]. For

geomaterials however, a linear model for cohesion degradation seems to fit experimental data well [98, 99].

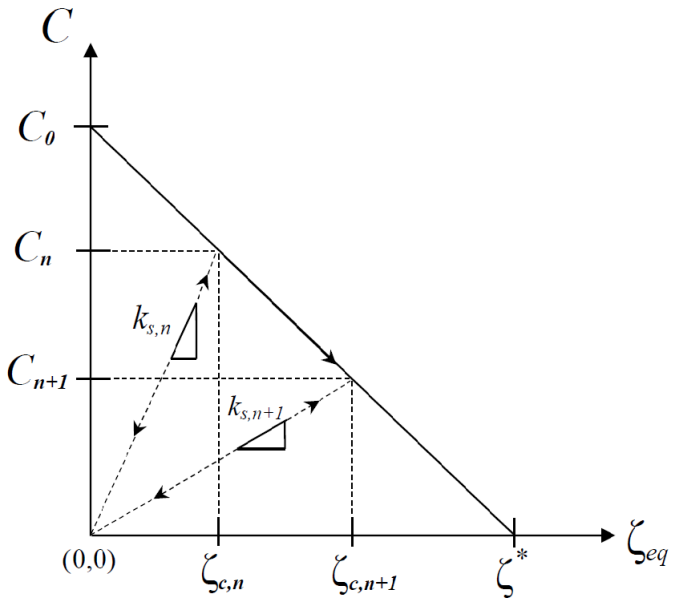

Figure 9: Cohesion softening law displaying different unloading-reloading curves at arbitrary time steps n and n+1

The initial cohesion is determined to be consistent with the bulk stress state at the moment of localization. In addition to linear softening we assume elastic unloading and reloading with respect to the equivalent traction and displacement.

We define a parameter $\zeta_c = \zeta^* (c_0 - c)/c_0$, which is the maximum equivalent slip magnitude observed on the slip surface up to the current time. The parameter k_s can be thought of as the

stiffness of the material and mathematically is defined as the slope of the unloading-reloading curve at a given value of ζ_c. Therefore, $k_s = c/\zeta_c$. On this portion of the curve, we also assume that the cohesion is frozen at its value which corresponds to ζ_c, thus the explicit form of k_s is given by

$$\begin{aligned} k_s &= c_0 \left(1 - \frac{\zeta_c}{\zeta^*}\right) \frac{1}{\zeta_c} \\ &= c_0 \left(\frac{1}{\zeta_c} - \frac{1}{\zeta^*}\right) \end{aligned} \tag{2.4.14}$$

Further softening on the band can only occur when $\zeta_{eq} \geq \zeta_c$.

Remark: The assumption that the cohesion is constant on the unloading-reloading portion of the graph is a simplification but also one which is grounded in reality. One could imagine that, under very small displacement values, as the crack moves back and forth, some material will remain intact although it will stretch or elongate. From a soils perspective, it is quite possible for clay material to undergo this process. For very small displacements, clay will deform but the overall cohesive force of the soil will remain intact.

2.5 Numerical Implementation of Slip Model

The solution technique employed to solve the slip at the element level is a piecewise Newton-Raphson iteration. This particular approach is well-suited for the proposed model due to the

fact that the combined opening-sliding model is accompanied by a nonlinear solution. An iterative scheme is also a good choice because it has the potential to capture a broader range of constitutive models that may be the focus of future investigation.

Unfortunately, it is not always possible a priori to determine whether the band is in compression or tension. This adds a non-smoothness to the equations that, in some cases, creates solution difficulties.

To this end, the slip parameter is solved using two distinct subroutines. One subroutine handles the case of positive normal traction on the band, thus solving for both opening and shear slip parameters. If the band is in compression (hence, zero normal slip on the band), a subroutine which solves solely for shear slip is utilized. If a change in the sign of the normal traction is detected within a given subroutine, then a new slip value is interpolated and used as the starting value in the appropriate subroutine. Doing this ensures that the Newton-Raphson is settling on the correct solution, given the traction state on the band.

The two subroutines differ in terms of which traction balance equations are utilized. Namely, when the band is in compression, only one equation is needed, which is the balance between the shear traction, friction and cohesive forces. In this case, the shear slip is solved for via the equation

$$\Phi = 0 = |\tau - k_s \zeta_s| - f. \tag{2.5.1}$$

Even if the N-R successfully yields a converged slip value, it must be ensured that the normal traction sign is negative (hence, the band is in compression) since it is possible for the band to go into a state of tension. This simply indicates that the slip on the band should instead be calculated using the combined opening-sliding formulation. In order to find the value of ζ_s at the onset of tension (hence, when $\sigma = \zeta_n = 0.0$) a standard linear interpolation is performed using Equation 2.5.2. We then use these new values of $\zeta_n = 0.0$ and ζ_s to initiate a N-R iteration in the opening-sliding subroutine (Equation 2.5.3 and Equation 2.5.4). The three points used for interpolation are as follows: (1) $\left(\sigma^i, \zeta_s^i\right)$, signify the initial normal traction and slip values at the beginning of the N-R iteration, (2) $(\sigma = 0.0, \zeta_s)$, the unknown value of ζ_s when the normal traction is zero and finally (3) $\left(\sigma_f, \zeta_s^f\right)$ which are the spurious converged values of the positive normal traction and the shear slip.

$$\zeta_s \quad = \quad \zeta_s^i - \sigma^i \cdot \left(\frac{\zeta_s^f - \zeta_s^i}{\sigma^f - \sigma^i} \right) \tag{2.5.2}$$

When the band is undergoing tension, the friction force is absent, and only the normal and shear traction forces need to balanced. Thus the following set of balance equations is simultaneously solved for the normal and shear slip values:

$$\Phi_1 = 0 = \sigma - k_n \zeta_n \tag{2.5.3}$$

$$\Phi_2 = 0 = \tau - k_s \zeta_s \tag{2.5.4}$$

$$\zeta_s = \zeta_s^i - \zeta_n^i \cdot \left(\frac{\zeta_s^f - \zeta_s^i}{\zeta_n^f - \zeta_n^i} \right) \tag{2.5.5}$$

Again, after convergence, the normal traction sign must be checked. If it is negative (hence the band should be in compression) then the normal slip, ζ_n, will also be negative, which is of course a spurious value. In this case, a new value for ζ_s is calculated using Equation 2.5.5, which is the value of the shear slip at the onset of compression (i.e., when $\sigma = \zeta_n = 0.0$). After this value is found, it is used as the initial start point for the N-R iteration in the sliding-only formulation (Equation 2.5.1).

The solution procedure for either formulation follows a standard Newton-Raphson approach given by

$$\boldsymbol{\zeta}_{n+1}^{k+1} = \boldsymbol{\zeta}_{n+1}^{k} - \left(\frac{\partial \boldsymbol{\Phi} \left(\zeta_{n+1}^{k} \right)}{\partial \boldsymbol{\zeta}_{n+1}^{k}} \right)^{-1} \boldsymbol{\Phi} \left(\zeta_{n+1}^{k} \right) \tag{2.5.6}$$

2.5.1 Slip Algorithm

The solution algorithm differs in form depending on whether the element is newly localized (in which case Box 2.5.1 is used) or if slip has already begun on the band (Box 2.5.1).

Box 1. Slip algorithm for a newly localized element.

Step 1: Compute $\boldsymbol{\sigma}_{n+1}^{tr} = \boldsymbol{\sigma}_n + \boldsymbol{c}^e : \Delta\boldsymbol{\epsilon}^{conf}$

Step 2: Check the traction on the band and enter the appropriate subroutine. First, assume elastic unloading/reloading on the band, hence hold k_s and k_n as constant and proceed to solve the balance equation(s).

If $\sigma > 0$ (tension) solve for ζ_n and ζ_s using equations

$\sigma - k_n\zeta_n = 0$

$\tau - k_s\zeta_s = 0$

Else ($\sigma < 0$, hence compression)

First, check for slip on the band:

If $|\tau - k_s\zeta_s| < f$

No slip on the band due to friction, exit with trial stress.

Else

Solve for ζ_s using: $|\tau - k_s\zeta_s| - f = 0$

After slip value(s) calculated in elastic unloading/reloading phase, check:

If $\zeta_{eq} < \zeta_c$

It is confirmed that the band is either unloading or reloading.

Therefore, update $\boldsymbol{\sigma}_{n+1}$ and set $\boldsymbol{\zeta}_{c,n+1} = \boldsymbol{\zeta}_{c,n}$ and exit.

Else

The band is in the softening phase. Recalculate the balance equation(s) allowing k_s and k_n to vary as in Box 2.5.1.

Additionally, interpolate as needed if the traction sign changes.

Step 3: Update $\boldsymbol{\zeta}_{n+1}$, $k_{s,n+1}$, $k_{n,n+1}$ and $\boldsymbol{\sigma}_{n+1}$ then exit.

Box 2. Slip algorithm for an element which has preexisting slip on the band.

Step 1: Compute $\boldsymbol{\sigma}_{n+1}^{tr} = \boldsymbol{\sigma}_n + \boldsymbol{c}^e : \Delta\boldsymbol{\epsilon}^{conf}$

Step 2: Check the traction on the band and enter the appropriate subroutine. First, assume elastic unloading/reloading on the band, hence hold k_s and k_n as constant and proceed to solve the balance equation(s).

If $\sigma > 0$ (tension) solve for ζ_n and ζ_s using equations

$\sigma - k_n\zeta_n = 0$

$\tau - k_s\zeta_s = 0$

Else ($\sigma < 0$, hence compression)

First, check for slip on the band:

If $|\tau - k_s\zeta_s| < f$

No slip on the band due to friction, exit with trial stress.

Else

Solve for ζ_s using: $|\tau - k_s\zeta_s| - f = 0$

After slip value(s) calculated in elastic unloading/reloading phase, check:

If $\zeta_{eq} < \zeta_c$

It is confirmed that the band is either

unloading or reloading. Therefore, update

$\boldsymbol{\sigma}_{n+1}$ and set $\boldsymbol{\zeta}_{c,n+1} = \boldsymbol{\zeta}_{c,n}$ and exit.

Else

The band is in the softening phase.

Recalculate the balance equation(s) allowing k_s and k_n

to vary as in Box 2.5.1. Additionally, interpolate as needed

if the traction sign changes.

Step 3: Update $\boldsymbol{\zeta}_{n+1}$, $k_{s,n+1}$, $k_{n,n+1}$ and $\boldsymbol{\sigma}_{n+1}$ then exit.

2.6 Stiffness Matrix Formulation

For the strong discontinuity approach, the resulting stiffness matrix from this formulation, assuming elastic unloading in the bulk material can be derived, following [57]. We begin with two sets of equations that must be solved: the standard balance of linear momentum (here taken to be quasi-static and small strain) and the traction balance on the localized deformation band.

$$\boldsymbol{r}^e = \int_{\Omega^e} \boldsymbol{B}^t : \boldsymbol{\sigma} \mathrm{d}\Omega - \int_{\Omega^e} \boldsymbol{N}^t \boldsymbol{b} \mathrm{d}\Omega - \int_{\Gamma^e} \boldsymbol{N}^t \boldsymbol{t} \mathrm{d}\Gamma = 0 \tag{2.6.1}$$

$$\boldsymbol{\Phi} = 0 \tag{2.6.2}$$

Taking variations on these, we arrive at

$$\delta \boldsymbol{r}^e = \boldsymbol{K}^e_{dd} \delta \boldsymbol{d}^e + \boldsymbol{K}^e_{d\zeta} \delta \boldsymbol{\zeta}^e \tag{2.6.3}$$

$$\delta \boldsymbol{\Phi} = \boldsymbol{K}^e_{\zeta d} \delta \boldsymbol{d}^e + \boldsymbol{K}^e_{\zeta\zeta} \delta \boldsymbol{\zeta}^e \tag{2.6.4}$$

where $\boldsymbol{K}^e_{dd}$ is the standard element stiffness matrix, and the others can be shown to have the following forms:

$$\boldsymbol{K}^e_{d\zeta} = -\int_{\Omega^e} \boldsymbol{B}^t : \boldsymbol{c}^e : \frac{\partial \boldsymbol{\epsilon}}{\partial \boldsymbol{\zeta}} \mathrm{d}\Omega \tag{2.6.5}$$

$$\boldsymbol{K}^e_{\zeta d} = \frac{\partial \boldsymbol{\Phi}}{\partial \boldsymbol{d}} = \frac{\partial \boldsymbol{\Phi}}{\partial \boldsymbol{\sigma}} : \boldsymbol{c}^e : \boldsymbol{B} \tag{2.6.6}$$

$$\boldsymbol{K}^e_{\zeta\zeta} = \frac{\partial \boldsymbol{\Phi}}{\partial \boldsymbol{\zeta}} \tag{2.6.7}$$

The tensor $\boldsymbol{B}$ is the third-order, symmetric gradient of the nodal displacement interpolation functions, commonly referred to as the strain-displacement tensor, i.e. $B_{ijk}d_k = \epsilon_{ij}$. The last equation is convenient because it is identical to the tangent stiffness used in the local N-R for determining the slip, and the same code can be reused. The other equations can be further specified

$$\frac{\partial \epsilon_{ij}}{\partial \boldsymbol{\zeta}} = \frac{1}{2} \begin{Bmatrix} \frac{\partial f^h}{\partial x_i} n_j + \frac{\partial f^h}{\partial x_j} n_i \\ \frac{\partial f^h}{\partial x_i} l_j + \frac{\partial f^h}{\partial x_j} l_i \end{Bmatrix} \tag{2.6.8}$$

where $\boldsymbol{\zeta} = \langle \zeta_n \ \zeta_s \rangle^t$.

Additionally,

$$\left(\frac{\partial \boldsymbol{\Phi}}{\partial \boldsymbol{\sigma}}\right)_{ijk} = \frac{\partial \Phi_i}{\partial \sigma_{jk}} \tag{2.6.9}$$

$$\frac{\partial \Phi_1}{\partial \boldsymbol{\sigma}} = \boldsymbol{n} \otimes \boldsymbol{n} \tag{2.6.10}$$

$$\frac{\partial \Phi_2}{\partial \boldsymbol{\sigma}} = (\boldsymbol{n} \otimes \boldsymbol{l})^s \tag{2.6.11}$$

The equations for the sliding-only case are as follows

$$\frac{\partial \epsilon_{ij}}{\partial \zeta_s} = \frac{1}{2}\left(\frac{\partial f^h}{\partial x_i} l_j + \frac{\partial f^h}{\partial x_j} l_i\right) \tag{2.6.12}$$

and

$$\frac{\partial \Phi}{\partial \boldsymbol{\sigma}} = (\boldsymbol{n} \otimes \boldsymbol{l})^s - sign\,(\sigma)\,\mu\,(\boldsymbol{n} \otimes \boldsymbol{n}) \tag{2.6.13}$$

For the quantities corresponding to $\frac{\partial \boldsymbol{\Phi}}{\partial \boldsymbol{\zeta}}$, refer to Appendix A.

The extra degrees of freedom may be condensed at the element level in the standard way, resulting in the final element stiffness matrix

$$\boldsymbol{K}^e = \boldsymbol{K}^e_{dd} - \boldsymbol{K}^e_{d\zeta} \boldsymbol{K}^e_{\zeta\zeta}{}^{-1} \boldsymbol{K}^e_{\zeta d} \tag{2.6.14}$$

2.6.1 Enhancing Simulation Robustness

In a comparative study of several different embedded discontinuity formulations, Jirasek [81] noted that even the most optimal enhanced finite element produces a global tangent stiffness matrix which is ill-conditioned and thus difficult to invert. Later, Jirasek and Belytschko in [100] compared the enhanced finite element method with the well-known extended finite element method (XFEM). While both methods suffer from robustness issues arising from material softening, the XFEM has fewer drawbacks than the embedded discontinuity formulation. However, in the latter framework, because of the more straight-forward implementation and the fact that the added degrees of freedom within localized elements can be statically condensed at the element level, considerable effort has been made to develop methods to circumvent the aforementioned robustness issues.

Although there are several remedies outlined in the literature, affording varying levels of success, a particular method which seems to be especially promising is an implicit-explicit integration technique, Impl-Ex, devised by Oliver and co-workers [52]. This method employs an implicit internal variable calculation at the end of the time step and on the subsequent time step, during the global N-R iteration, these values are used in a semi-implicit calculation of the stresses. The benefit of this method is that for the semi-implicit calculation a positive definite stiffness matrix results which affords the simulation significant gains with regard to robustness.

Impl-Ex Integration Method

For a given localized element, the internal variables such as plastic slip magnitude are calculated implicitly at the end of the time step, after the convergent solution of the global displacements is obtained. Typically, on the subsequent step during the global N-R iteration, the stress in a localized element is calculated using, again, a fully implicit calculation. In contrast, for the Impl-Ex method, the stress is calculated semi-implicitly, which means that the previously obtained implicit values from the prior time step are used as either semi-implicit or explicit values. The general form of the semi-implicit stress, which is recognizable as the standard predictor-corrector form used in stress return plasticity algorithms, is given in Oliver by

$$\tilde{\boldsymbol{\sigma}}_{n+1} = \boldsymbol{\sigma}_n + \boldsymbol{c}^e : \Delta\boldsymbol{\epsilon}_{n+1} - \Delta\tilde{\lambda}_{n+1}\boldsymbol{c}^e : \frac{\partial g\left(\tilde{\boldsymbol{\sigma}}_{n+1}\right)}{\partial\tilde{\boldsymbol{\sigma}}_{n+1}} \tag{2.6.15}$$

Using an explicit approximation of the plastic multiplier term we have

$$\tilde{\lambda}_{n+1} = \lambda_n + \frac{\Delta t_{n+1}}{\Delta t_n}\Delta\lambda_n \tag{2.6.16}$$

where

$$\Delta\lambda_n \quad = \quad \lambda_n - \lambda_{n-1}. \tag{2.6.17}$$

λ_n is the value of the previous time step's plastic multiplier; it is calculated implicitly after convergence of the global N-R. Similarly, λ_{n-1} is the implicit value from the nth minus one time step. Thus, in the current time step that $\Delta\lambda_n$ is being used, it is an explicit value.

Taking the derivative of the semi-implicit stress with respect to the current strain, we obtain the so-called effective algorithmic operator

$$\boldsymbol{C}^{\text{eff}}_{n+1} \quad = \quad \frac{\partial\tilde{\boldsymbol{\sigma}}_{n+1}}{\partial\boldsymbol{\epsilon}_{n+1}} = \left(\boldsymbol{I} + \Delta\tilde{\lambda}_{n+1}\boldsymbol{c}^e : \tilde{\boldsymbol{A}}_{n+1}\right)^{-1} : \boldsymbol{c}^e \tag{2.6.18}$$

$$\tilde{\boldsymbol{A}}_{n+1} = \frac{\partial^2 g\left(\tilde{\boldsymbol{\sigma}}_{n+1}\right)}{\partial\tilde{\boldsymbol{\sigma}}_{n+1} \otimes \tilde{\boldsymbol{\sigma}}_{n+1}} \tag{2.6.19}$$

(Refer to Appendix B for a derivation of the effective algorithmic operator.) In applying the Impl-ex method to our particular formulation, the semi-implicit stress is calculated accordingly:

$$\tilde{\boldsymbol{\sigma}}_{n+1} = \boldsymbol{\sigma}_n + \boldsymbol{c}^e : \Delta\boldsymbol{\epsilon}^{\text{conf}}_{n+1} - \boldsymbol{c}^e : \left(\Delta\tilde{\boldsymbol{\zeta}}_{n+1} \otimes \nabla f^h\right)^s \tag{2.6.20}$$

where

$$\tilde{\boldsymbol{\zeta}}_{n+1} = \left[\left(\zeta_n + \frac{\Delta t_{n+1}}{\Delta t_n}\Delta\zeta_n\right)\boldsymbol{n} + \left(\zeta_s + \frac{\Delta t_{n+1}}{\Delta t_n}\Delta\zeta_s\right)\boldsymbol{l}\right]_{n+1} \tag{2.6.21}$$

For the effective operator calculation, we need the explicit form of the plastic potential term. If we define the direction of the slip on the deformation band as $\hat{\boldsymbol{\zeta}}$, we have for the potential

$$\frac{\partial g\left(\tilde{\boldsymbol{\sigma}}_{n+1}\right)}{\partial\tilde{\boldsymbol{\sigma}}_{n+1}} = \hat{\boldsymbol{\zeta}}_{n+1} \otimes \nabla f^h_{n+1} \tag{2.6.22}$$

The explicit form is not necessary however, since $\hat{\boldsymbol{\zeta}}_{n+1} \otimes \nabla f^h_{n+1}$ is calculated during the previous time step. In this case, we freeze not only the magnitude but the direction of $\hat{\boldsymbol{\zeta}}_{n+1}$. In the current time step, then, it is explicitly known and thus, $\boldsymbol{A}_{n+1} = 0$. Therefore, the jump in the displacement field is determined from the previous time step. Hence, the effective operator reduces to

$$\boldsymbol{C}_{n+1}^{\text{eff}} \quad = \quad \boldsymbol{I} : \boldsymbol{c}^e = \boldsymbol{c}^e \tag{2.6.23}$$

Hence, while there is a slight loss of accuracy in the added assumption, a simpler formulation is recovered that is linear in the case of linear elasticity. This fact tends to improve convergence rates in examples. On a concluding note, while the Impl-Ex method provides tremendous gains in terms of numerical robustness and tractability, especially for problems with complex geometries, the drawback of this method is that accuracy is sacrificed due to the semi-implicit calculation on the global step. Fortunately though, the remedy lies in simply choosing a sufficiently small time step such that the error is kept within acceptable bounds. In the numerical results section we show that with a small enough step size, the Impl-Ex produces results comparable to that of the fully implicit formulation.

2.7 Numerical Examples

Four numerical examples are presented here as a comparison of the sliding model versus the combined sliding-opening model.

2.7.1 Plane strain compression and tension of a column using a uniform load

2.7.1.1 Plane strain compression test

The first example is a pressure-confined column subjected to a uniform displacement (Figure Figure 10). The loading is quasi-static, hence inertial effects are neglected. The bottom of the

specimen is fixed so that it cannot translate vertically. In addition to this, one node is fixed horizontally so that the specimen is allowed to expand laterally. A confining pressure of 25 MPa is applied to the nodes on both sides of the specimen. The pressure is applied at the onset of the simulation resulting in a uniform stress state throughout the mesh. This stress state causes all of the elements to localize in the same time step. This being the case, a seed element has to be chosen so that one dominant band will propagate throughout the mesh. When this initial element localizes, the band tracking algorithm will generate a single band from the seed element at the critical orientation and terminate at the opposite end of the mesh.

TABLE I: MATERIAL PARAMETERS FOR PLAIN STRAIN COMPRESSION SAMPLE

Parameter	Symbol	Value
Young's Modulus	E	5500 MPa
Poisson's Ratio	ν	0.25
Cohesive Strength Parameter	α	8.034 MPa
Friction Parameter	β	0.633
Dilation Parameter	b	0.633
Hardening Modulus	H	-10 MPa
Localized Friction Coefficient	μ	0.72
Characteristic Slip Distance	ζ^*	0.5 mm

The reaction force graph shows a characteristic elastic response as the material resists deformation, followed by a brief plastic response and then failure. In quasi-brittle and rock-like

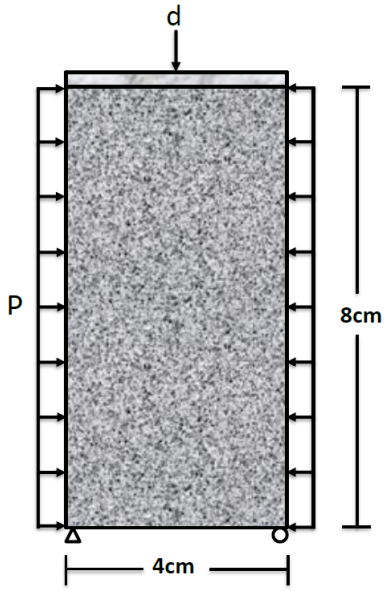

Figure 10: Geometry and loading for plane strain compression model. Simple constraints on the bottom allowing lateral expansion.

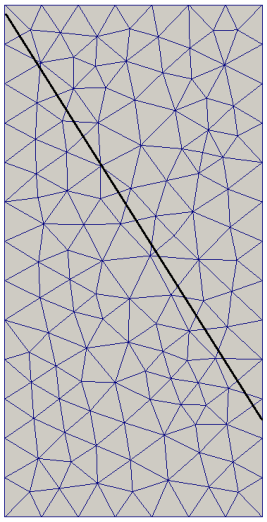

Figure 11: Discretized mesh of the triaxial tested specimen showing the propagating deformation band through elements.

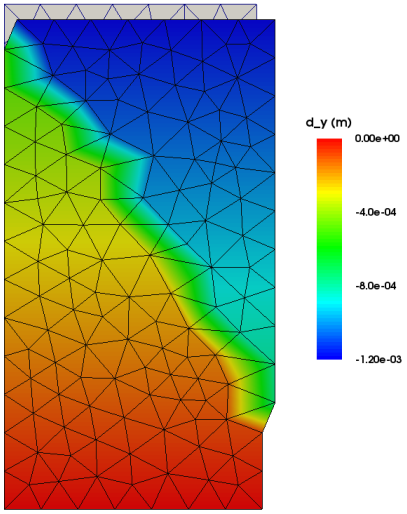

Figure 12: Specimen showing localized deformation along slip plane.

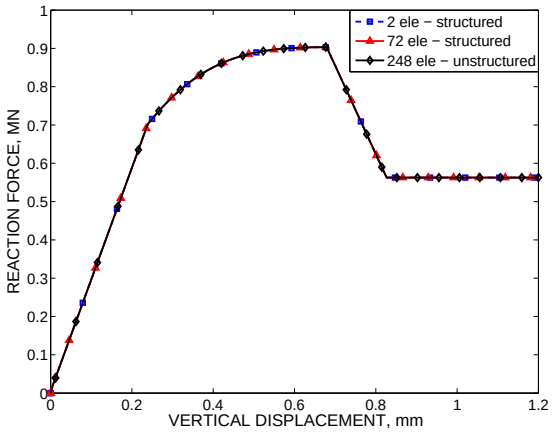

Figure 13: The graph shows the characteristic elastic and plastic responses as well as a stress drop and a constant frictional response.

materials, at low confining stresses, a narrow plastic region is expected due to the low ductility. After plasticity, failure occurs in which deformation in the localized elements is concentrated solely on the slip surface while the bulk material of the element unloads elastically. After the cohesion is fully degraded a constant friction force response is observed. Both the combined and sliding-only formulations produce identical results. This is to be expected since in a purely compressive state, both formulations simplify to the sliding Mohr-Coulomb law with friction.

2.7.1.2 Tension test for plain-strain sample

In this example, we reverse the direction of the displacement loading and retain the confining forces on the specimen, thus creating a uniform stress in the vertical direction. As is expected, the reversal of the displacement produces a slip line that is oriented 30 degrees from the horizontal plane. From the reaction force profiles, the sliding-only formulation softens more quickly than the combined opening-sliding formulation due to the fact that it only needs to overcome cohesive forces in one direction, namely parallel to the deformation band. In contrast, the combined formulation must overcome cohesion both normal and parallel to the band. The deformation graphs reveal that although the sliding-only simulation terminates earlier, more deformation is seen in the x direction than in the combined formulation. This makes sense because in the absence of an opening degree of freedom, the specimen undergoes increased deformation in the direction parallel to the band. When the cohesion degrades to zero, both

simulations fail to converge because the system becomes under-constrained (i.e., the top half of the sample has no displacement constraints in the x-direction).

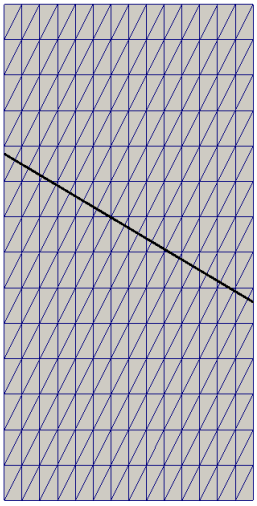

Figure 14: For the column in tension, the deformation band is now oriented 30 degrees from the horizontal plane.

2.7.2 Sample with hole subjected to shearing load

The next example, which features a slightly more complex geometrical figure, showcases the versatility that is gained when the added opening degree of freedom is employed. As mentioned previously, Foster et al [57] showed that the formulation involving the single degree of freedom led to spurious, mesh-dependent results. Namely, because the elements with different sliding directions are impeded by each other, stress build-up occurs around the localization zone.

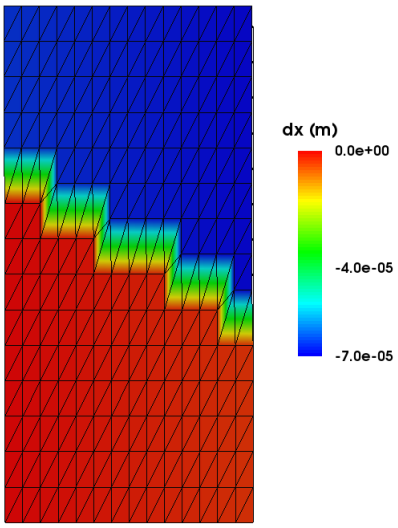

Figure 15: The opening-sliding formulation shows relatively less horizontal sliding than the sliding-only formulation.

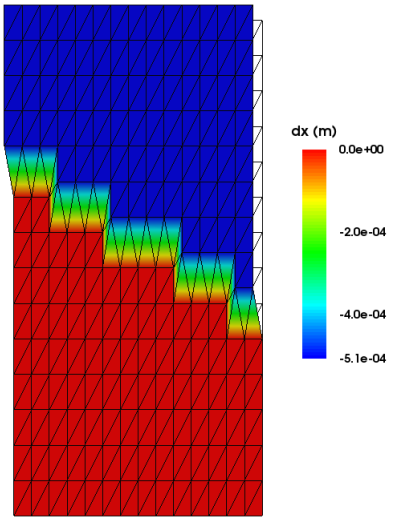

Figure 16: The sliding-only formulation causes significant horizontal deformation due to the lack of the opening degree of freedom.

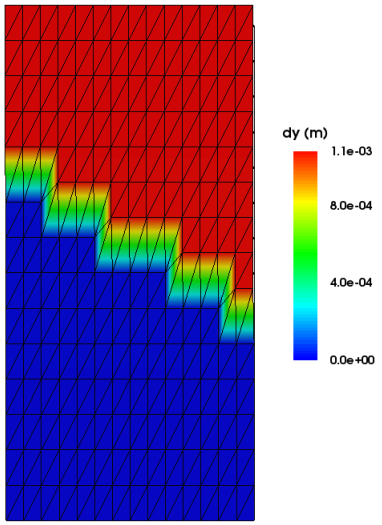

Figure 17: The opening degree of freedom allows the slip normal to the deformation band to be the dominant mode of slippage.

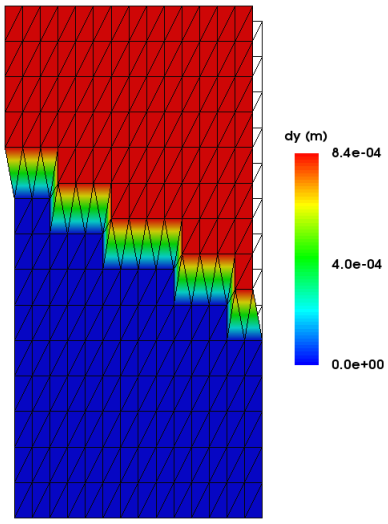

Figure 18: The vertical displacement for the sliding-only formulation is minimal compared to that of the opening-sliding formulation.

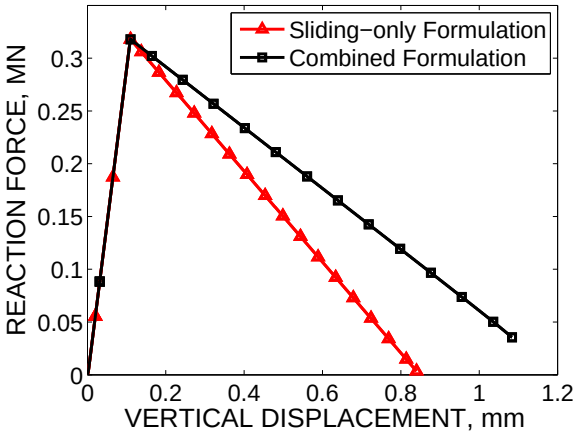

Figure 19: Both simulations fail to converge once the cohesion reaches zero. The sliding-only case softens quicker because the cohesion only acts parallel to the deformation band whereas opening-sliding formulation presents cohesion both normal and parallel to the band.

For the shearing example, in the case of the sliding-only formulation, multiple bands form (Figure 22), which produce significant locking and subsequent hardening. Notice that due to this stress build-up, neither band is able to fully propagate. Figure Figure 24 shows a distinctive kink in the reaction force which arises due to the hardening around the localization zone. In contrast, for the combined formulation one fully formed band (Figure 21), on each side, occurs which is concomitant with a significant stress drop in the material. For higher mesh refinements, after the cohesion completely degrades, there is a slight rise in the reaction force (Figure 27) which is due, not to geometric locking, but rather to more complex deformation patterns induced by the addition of more sampling points. This, in turn, produces an impediment to slippage, particularly at the corners where high compression is observed, resulting in the increase of shear resistance seen at the tail end of the softening curve. The final case (Figure 23) features

elements which are embedded with a predefined strong discontinuity. This case was added to show that completely horizontal bands will produce a response in which the stress in the sample is completely released by the proliferation of fracture; in the absence of band curvature, the sample is allowed to freely translate in the horizontal direction.

TABLE II: MATERIAL PARAMETERS FOR SAMPLE WITH HOLE

Parameter	Symbol	Value
Young's Modulus	E	9000 MPa
Poisson's Ratio	ν	0.15
Cohesive Strength Parameter	α	8.034 MPa
Friction Parameter	β	0.633
Dilation Parameter	b	0.3165
Localized Friction Coefficient	μ	0.60
Localized Hardening Modulus	H	0.0 MPa
Characteristic Slip Distance	ζ^*	0.5 mm

Figure 28-Figure 31 show a comparison between the Impl-Ex and fully implicit integration schemes for the shearing example with a hole (utilizing the sliding-only formulation), comprised of 288 elements. For Δt = 1.0e-2 (a) the Impl-Ex shows noticeable oscillation, particularly at the peak and when the cohesion is significantly degraded. As the time step is refined, e.g. in the cases of Δt = 2.0e-3 (b) and Δt = 1.0e-3 (c) the Impl-Ex method is able to navigate these areas more adeptly. And in the final case of Δt = 2.0e-4 (d) the oscillation is mitigated to the point that it essentially becomes negligible. Though the time step needed for the Impl-Ex is

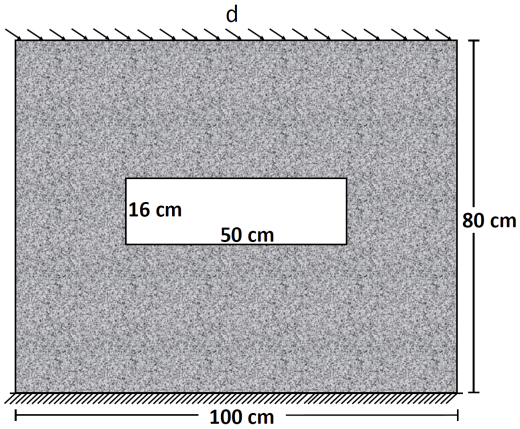

Figure 20: Boundary conditions for sample with a rectangular hole. There is a dominant shear displacement being applied to the top and a small vertical displacement which keeps the specimen from undergoing significant rotation after localization.

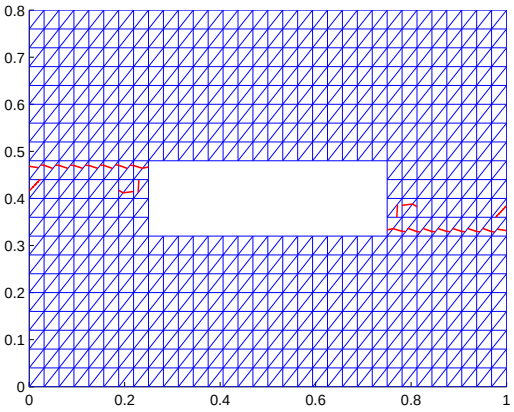

Figure 21: For the opening-sliding model one dominant band is able to propagate, thereby releasing stress in the entire specimen.

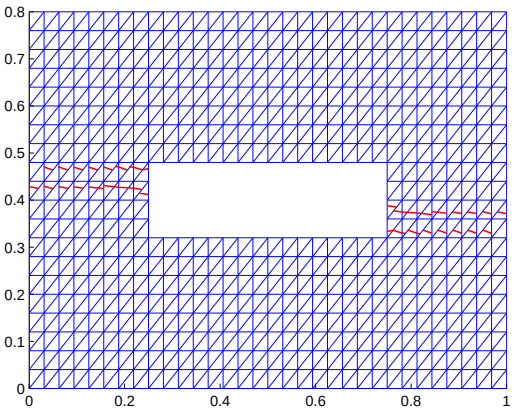

Figure 22: The sliding-only model gives rise to two bands both which experience locking which is accompanied by a high concentration of stress.

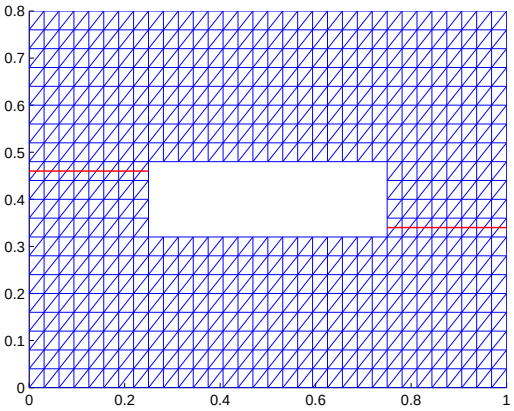

Figure 23: This figure depicts a predefined, straight deformation band along with .

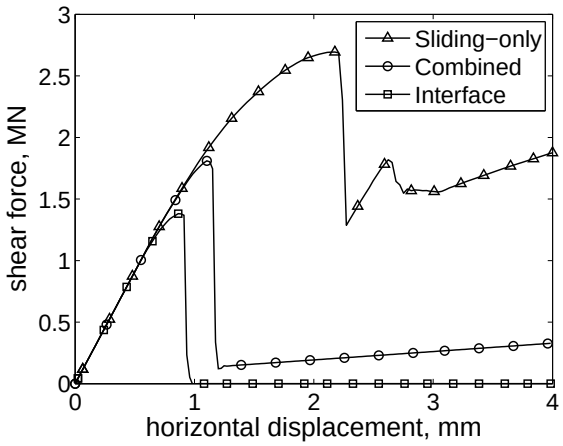

Figure 24: The sliding-only formulation shows locking resulting in multiple bands, whereas the combined sliding-opening formulation shows a significant stress drop and a subsequent slight increase in stress due to the rotation of the sample. The horizontal, pre-embedded discontinuity surfaces help the sample to avoid rotating and thus allows the stress to completely degrade. All results are from a mesh comprised of 576 elements.

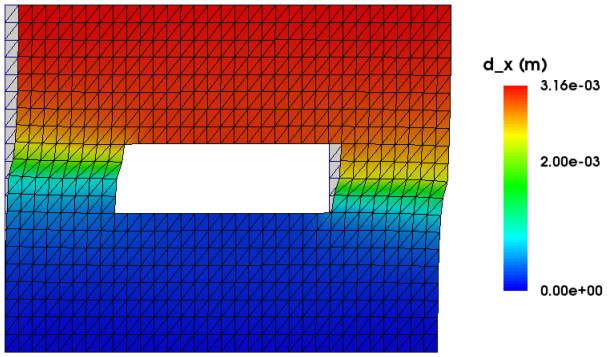

Figure 25: For the sliding-only formulation, two competing bands form and geometric locking ensues which produces a significant build up of bulk plasticity around the fracture zone.

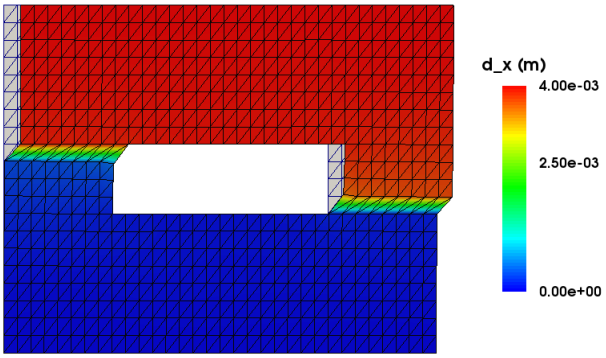

Figure 26: In the opening-sliding formulation (b), one dominant area of localization on each side of the specimen occurs, along which stress is released.

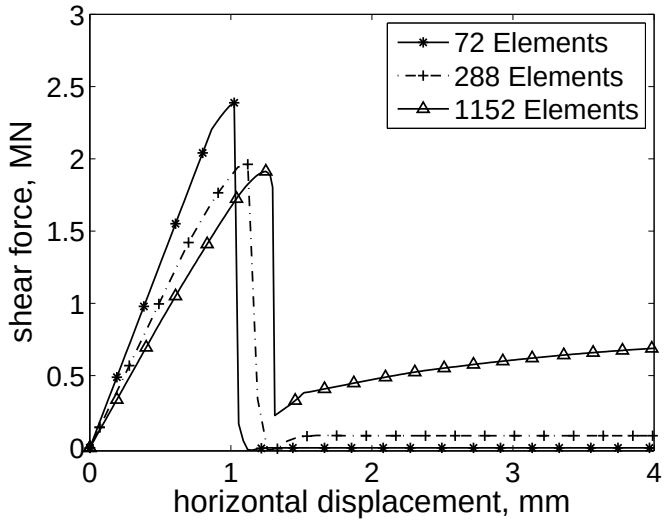

Figure 27: Convergence test for the plate with the hole run with the combined open-sliding formulation. The finest mesh shows a significant rise in the reaction force due to the more accurate calculation of the concentrated stress field around the corners of the hole.

significantly smaller than that of the fully implicit scheme, it is far more robust. Additionally, because the elastic modulus is used as the effective tangent operator (which is trivially simply to invert) the simulation runs significantly faster than that of the fully implicit scheme. What is also notable is that the fully implicit is quite sensitive to the value of the critical slip parameter; if the material softens too quickly, this scheme has difficulty in capturing this quick descent and thus fails to converge. In contrast, because the Impl-Ex produces a positive-definite local stiffness matrix, it is not sensitive to how quickly the material softens.

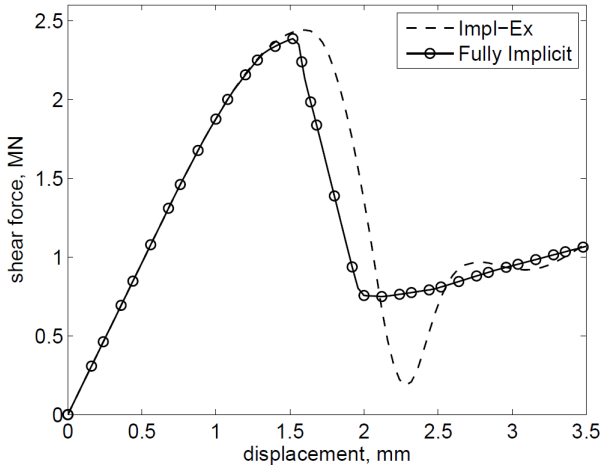

Figure 28: With $\Delta t = 1.0e\text{-}2$, the Impl-ex shows noticeable oscillation when the cohesion completely degrades. The instability caused by the non-smooth transition to zero cohesion is amplified by the explicit step of the integration scheme.

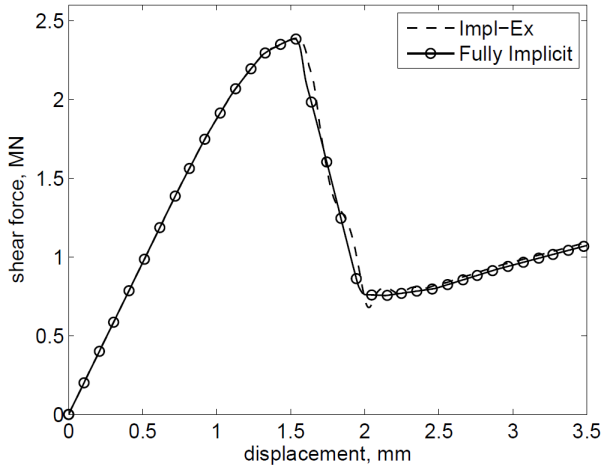

Figure 29: Reducing the time step by half an order of magnitude to Δt = 2.0e-3 significantly reduces the oscillation in the Impl-Ex scheme.

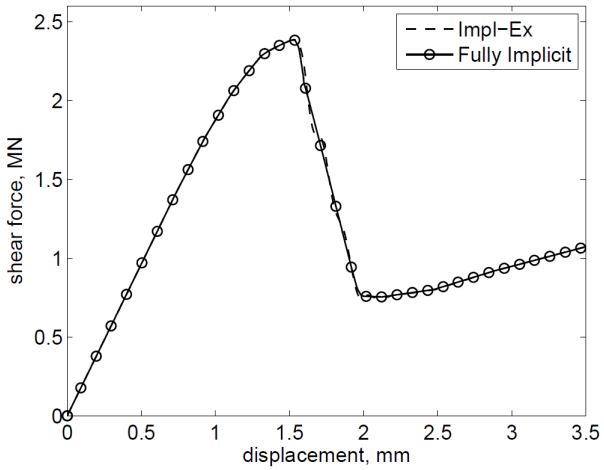

Figure 30: Halving the previous time step to Δt = 1.0e-3 almost makes the oscillation unnoticeable.

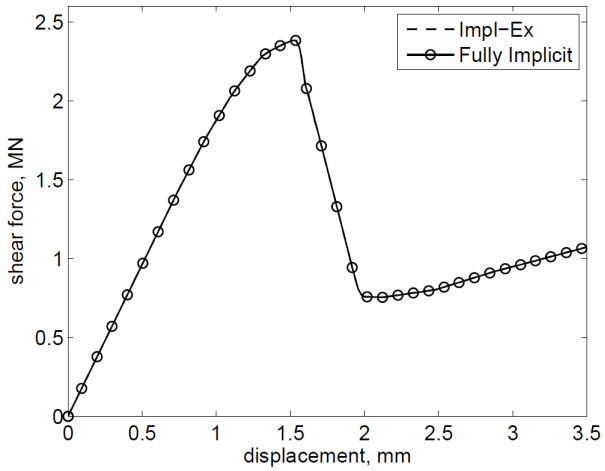

Figure 31: For a near-complete smooth curve, the time step is reduced by a half order of magnitude to Δt = 2.0e-4.

2.7.3 Slope stability

This particular example is motivated by and thus similar to the one detailed in [54]. This example was chosen because it presents a very complex mix of interactions, such as high compression, tension, friction and rotation. At the top of the slope is a rigid embankment which is comprised of elements that are only allowed to undergo elastic deformation; plasticity and localized behavior are excluded. This is to prevent these elements from localizing so that softening behavior is solely relegated to the underlying material, which is the main area of interest. Figure Figure 33 shows a comparison of the localization lines which illustrates the differing angle of decent between the two formulations. The combined formulation produces a more shallow angle. This can be understood in that the opening degree of freedom allows the material to undergo a significant amount of softening, over that of the single degree formulation, and hence

less stress build-up occurs. In contrast, because geometric locking occurs in the sliding-only case, the resulting stress increase causes a steeper localization angle, more friction resistance and ultimately locking.

In addition, a significant amount of rotation is seen in the combined case because the opening degree of freedom allows the material to move much more freely than in the sliding-only case.

TABLE III: MATERIAL PARAMETERS FOR SLOPE STABILITY EXAMPLE

Parameter	Symbol	Value
Young's Modulus	E	10 MPa
Poisson's Ratio	ν	0.4
Cohesive Strength Parameter	α	40 KPa
Friction Parameter	β	0.3
Dilation Parameter	b	0.06
Localized Friction Angle	ϕ	10°
Localized Hardening Modulus	H	0.0 MPa
Characteristic Slip Distance	ζ^*	0.4 m

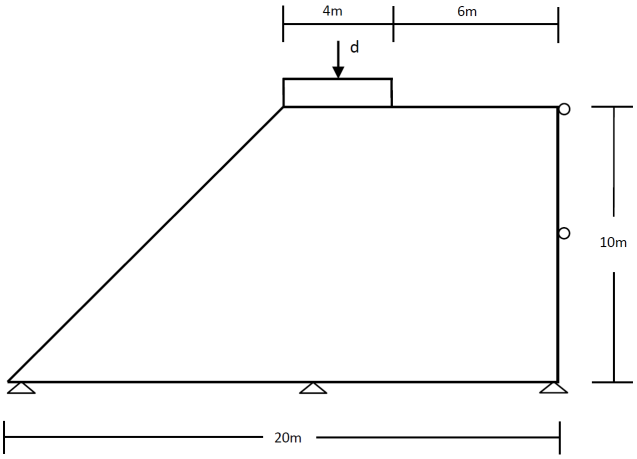

Figure 32: Slope stability problem with point load applied at midpoint of rigid embankment, full constraints on the bottom and constraints in the horizontal direction on the far right side.

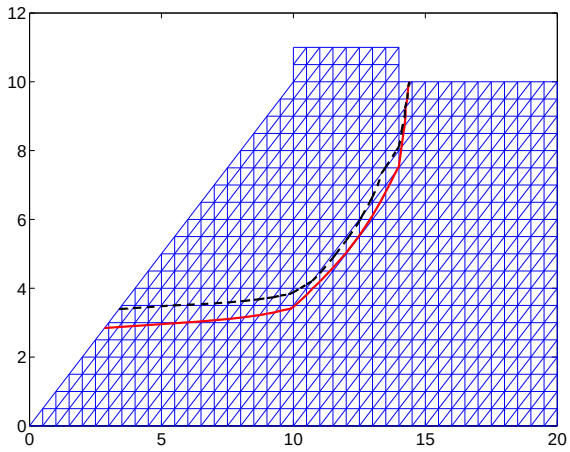

Figure 33: Comparison of the slip lines; the dotted black line corresponds to the opening-sliding formulation and the red line corresponds to the sliding-only formulation. The opening-sliding formulation produces a more shallow descent angle because the stress is released sooner than that of the sliding-only formulation.

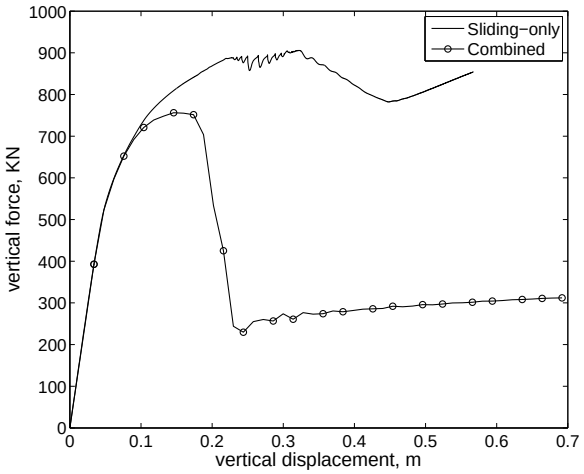

Figure 34: In the sliding-only case, there is significant friction resistance as well as locking and subsequent stress build-up. The opening-sliding formulation shows a large stress drop and resistance due to the slope rotation after complete cohesion degradation.

2.8 Conclusions

In simulating the initiation and propagation of localized deformation, the combined opening-sliding constitutive model alleviates the spurious geometric locking effect seen in the prior model which featured only a single sliding degree. Through several benchmark examples, the combined formulation displays expected softening as well as offers more accurate solutions, particularly in the case of pure tension. Also, the formulation shows its versatility in large-scale problems as seen in the slope stability example. Lastly, implementation of the Impl-Ex technique affords the simulation code significant increases in convergence and robustness. With this in hand,

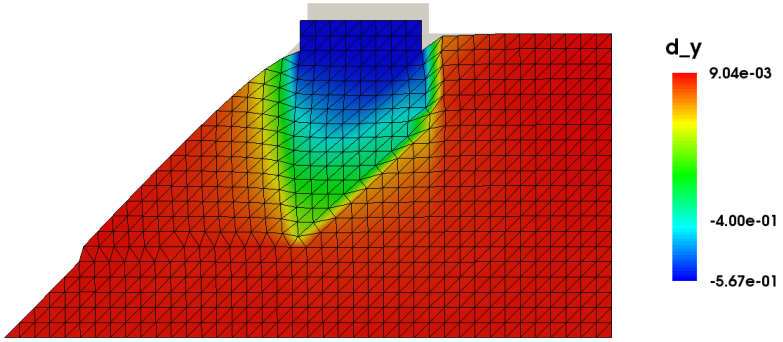

Figure 35: The downward motion of the soil is impeded by an arrest of slippage for the sliding-only formulation.

the next logical step is to expand the simulations into the three-dimensional realm in order to simulate more realistic situations within a geomechanics context.

Future studies will also include the combination of the this model with a plasticity model suited for geomaterials, which is detailed in [90]. The two models will be combined using the formulations outlined in [101]. In addition to this, the variable friction model in [57] can be incorporated so as to more accurately capture the friction behavior of geomaterials.

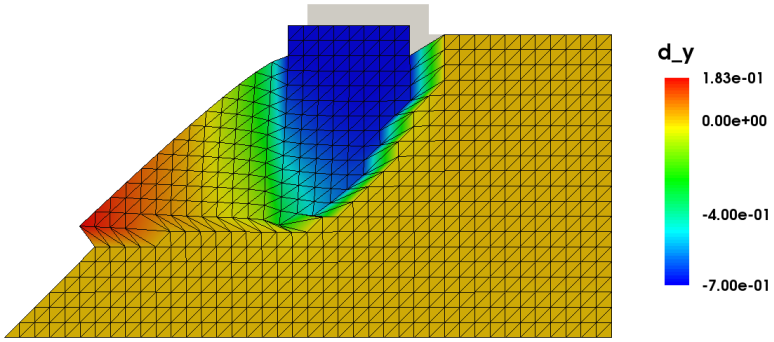

Figure 36: The opening-sliding formulation displays a large amount of rotation in the slipping soil.

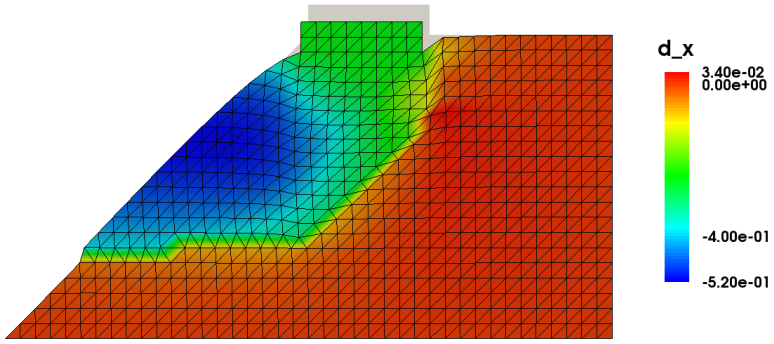

Figure 37: The sliding-only formulation does not allow the soil to translate horizontally due to a build-up of friction and stress along the interface.

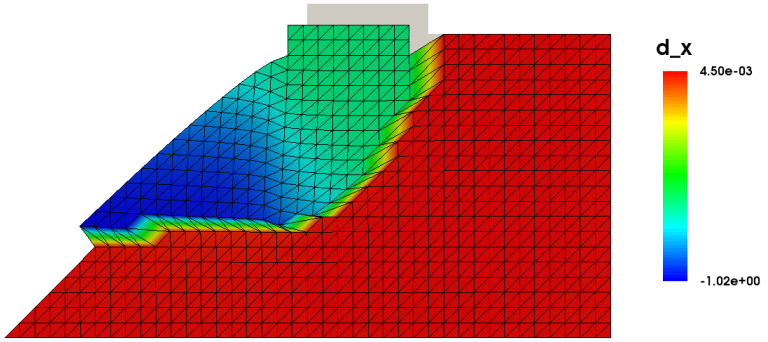

Figure 38: In the opening-sliding formulation, the cohesion completely degrades and thus significant horizontal deformation is seen.

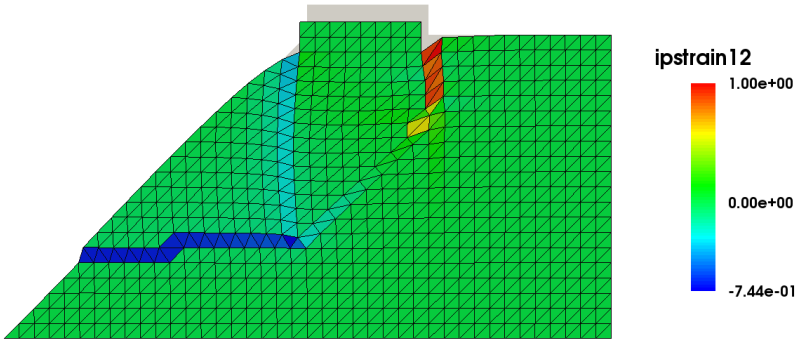

Figure 39: The stress build-up in the sliding-only formulation causes two bands to begin to nucleate at the foot of the embankment

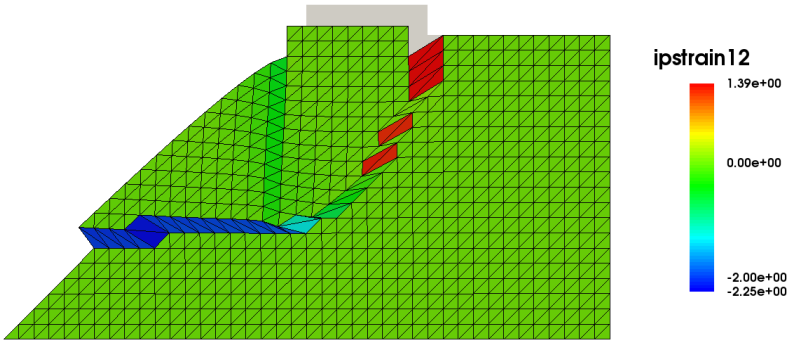

Figure 40: In the opening-sliding formulation, though there is noticeable shear stress on the left side of the embankment, most of the shear stress is released along the deformation band on the right side.

CHAPTER 3

A NEW METHOD FOR EMBEDDING PRE-DEFINED INTERFACES IN FINITE ELEMENTS

3.1 Introduction

The presence of weak interfaces within materials may hold significant ramifications for their overall performance. These interfaces often introduce orthotropic or anisotropic characteristics into structures and reduce their load-carrying capacity. Some common scenarios in which interfaces are present involve delamination between composites, soil-reinforcement interaction, rock joint analysis, and masonry, among others. Given the importance of these applications, a number of approaches to modeling interfaces within a finite element context has arisen over the years. Typically, most of the current approaches draw from several benchmark approaches. Gens and coworkers [102] list a brief categorization of these approaches, which fall into three major categories: interfaces modeled using standard elements of finite thickness, quasi-continuum elements possessing weak planes in the direction of the interface or joint, and nodal elements (placed at the boundaries of continuum elements) which have zero width. Some have also proposed spring elements, which behave very similarly to zero-width finite elements.

The advantage of zero-width elements is that they can be inserted between element boundaries, lending to a very sharp resolution and distinct boundary between two materials. This is ideal

for composite materials and simulating delamination [24, 63, 103]. The drawback is that these elements must be given an initial high artificial stiffness so that they do not undergo significant deformation under large elastic loads. This introduces spurious oscillations into the finite element solution, which however has been remedied in [104]. Complex patterns of interfaces, such as those found in joint sets in rock, can also make meshing the interfaces significantly challenging. Another factor is that zero-width elements differ in terms of shape function structure than their neighboring continuum elements. The advantage of using continuum elements which are embedded with weak planes is that a single form of the shape functions can be used for all elements. Additionally, these can be designed in such a way that a high initial stiffness is not needed to prevent deformation.

The approach outlined in this chapter incorporates the use of a continuum element embedded with a weak plane, which will serve as an interface. This method was conceptualized by Foster and coworkers in [57] while investigating variable friction rates in geomaterials. The method in this chapter follows their concepts and extends them to an algorithmic procedure which can propagate interfaces at any orientation in a given finite element mesh. Furthermore, these interfaces possess properties such as a friction coefficient, initial cohesive strength, and parameters related to a given material's energy release rate or stress intensity factors. These interfaces are cast in the framework of embedded discontinuities suited for capturing highly localized strain, closely following the form contained in [54, 57, 58, 82], among others. A favorable feature of this framework is that the nodal degrees of freedom for the interfaces are local to a given element

and thus can be condensed out of the global system of finite element equations, thereby saving computational costs and algorithmic complexity.

This chapter is structured as follows: In Section 2, the kinematics and finite element formulation are briefly outlined. Section 3 details the procedure for embedding and propagating interfaces within a finite element mesh. Section 4 presents the yield criteria for the interfaces, based on a traction-separation law suited for both compressive and tensile states. Section 5 shows numerical results of examples featuring periodic masonry found in the literature (see [34, 105]). Section 6 closes with remarks drawn from analyses of the examples as well as future work.

3.2 Interface Formulation

The predefined interfaces are modeled as embedded strong discontinuities and thus are governed by the same kinematics as the embedded discontinuities detailed prior in Section 2.2.1. Hence, the displacement field is

$$\boldsymbol{u} := \bar{\boldsymbol{u}} + [\![\boldsymbol{u}]\!] H_S(\boldsymbol{x}), [\![\boldsymbol{u}]\!] = \boldsymbol{\zeta} = \zeta_s \boldsymbol{l} + \zeta_n \boldsymbol{n} \tag{3.2.1}$$

Furthermore, the finite element implementation is identical to that detailed in Section 2.3. Therefore, for an element experiencing a displacement jump along the interface, a conforming displacement field can be derived that will conform to the standard finite element shape functions (Figure 41). Also, the sets of active (AN) and inactive (IN) nodes, which designate

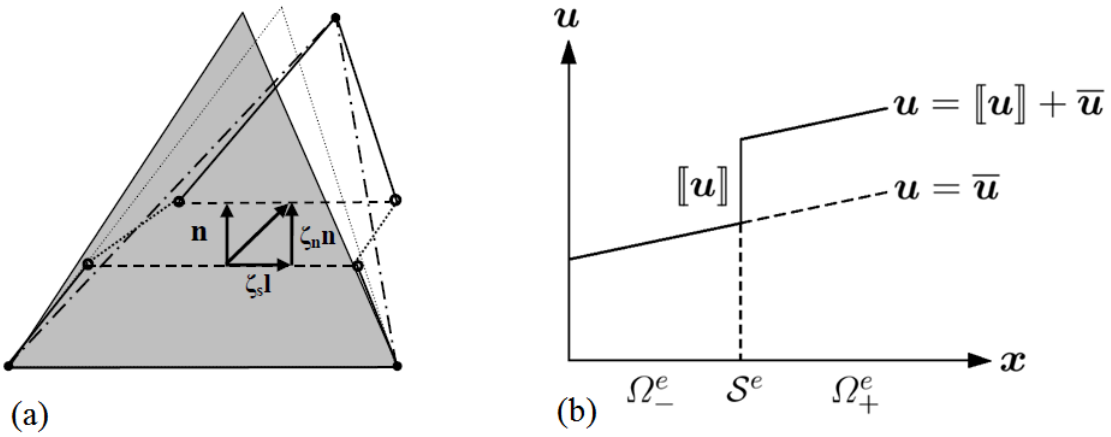

Figure 41: (a) CST experiencing a displacement jump, $\boldsymbol{\zeta}$, along a predefined interface. The bold, horizontal dashed line represents the interface, the faint dotted line is the deformed shape, and the dash-dotted line represents the conforming displacement field of the element. (b) Total displacement field for CST experiencing continuous deformation and displacement jump.

the node(s) that receives the displacement contribution from the jump, are allocated by the function f^h defined in Equation 2.3.3.

The orientation of the interface is a predefined unit vector, $\boldsymbol{l}$, which also serves as the direction for the tangential slip, ζ_s. This orientation is the slope of the line defined by the two points, $(x_1,\ y_1)$ and $(x_2,\ y_2)$, which are user-defined inputs. The algorithm for embedding these interfaces is the subject of the following section.

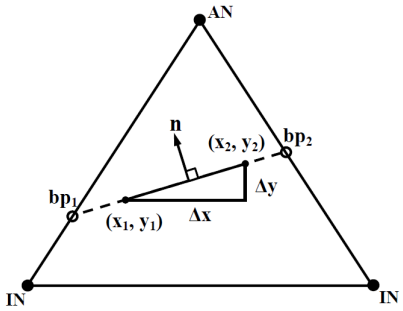

Figure 42: Element with embedded interface and band points (edge coordinates). The orientation of the band is defined by user inputs, $(x_1,\ y_1)$ and $(x_2,\ y_2)$.

3.3 Predefined Interface Embedding Procedure and Algorithm

3.3.1 Edge point algorithm

In order to propagate interfaces throughout a finite element mesh, precisely where the interfaces intersect the edges of elements within the mesh must be determined. In order to find these intersection points, we employ the edge-detecting algorithm developed in [57]. Given the orientation of an interface, $\boldsymbol{l}$, a point on the band, $\mathbf{x}_s^e$, and the coordinate end nodes of an edge, $\mathbf{x}_a^e$ and $\mathbf{x}_b^e$, a system of equations can be constructed and solved to determine where the band intersects the edges of an element (Figure 43). This algorithm is summarized in Box 2.

$$\mathbf{x} = \mathbf{x}_s^e + \alpha \mathbf{l} \tag{3.3.1}$$

$$\mathbf{x} = \beta \left(\mathbf{x}_a^e - \mathbf{x}_b^e \right) \tag{3.3.2}$$

where α and β are unknown scalars. After these equations are solved for α (Equation 3.3.3), this value is substituted into Equation 3.3.1 in order to find the intersection point, $\mathbf{x}$.

$$\alpha = \frac{|| \left(\mathbf{x}_a^e - \mathbf{x}_b^e\right) \times \left(\mathbf{x}_s^e - \mathbf{x}_b^e\right) ||}{||\mathbf{l} \times \left(\mathbf{x}_a^e - \mathbf{x}_b^e\right) ||} \tag{3.3.3}$$

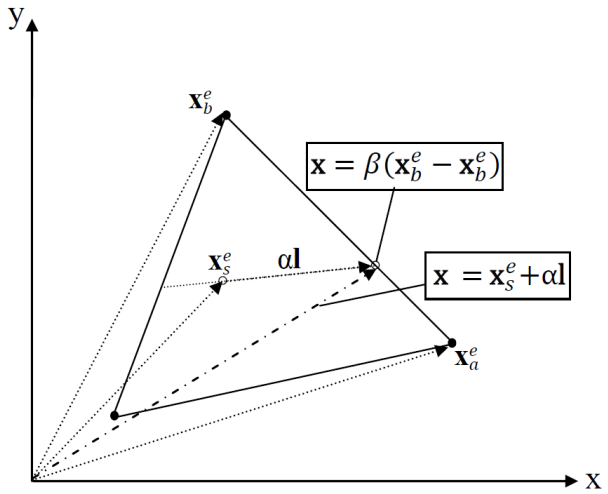

Figure 43: Vectorial depiction of the edge-finding method.

It must be mentioned that for the first element which is to have an interface embedded into it, the point on the band, $\mathbf{x}_s^e$, will not be one of the known edge coordinates (like it is for all subsequent elements that have interfaces embedded into them). This means that in order

to solve for α in the first element, we need a method to find $\mathbf{x}_s^e$. One way to do this would be to design the algorithm so that the user specifies the first element that the interface will begin to propagate through. Once this element is known, the centroid of the element can be designated as $\mathbf{x}_s^e$. However, it may be cumbersome to choose a specific element especially if one needs to repeatedly refine or reconfigure the mesh in a given way. The algorithm in this study is designed such that if the user specifies the global coordinates where the interface is to begin, then a separate algorithm will be invoked which locates the element in which those global coordinates lie. This way, no matter how the mesh is readjusted, the interface will begin and propagate from the same general area (and terminate in the same area as well).

One can devise a number of ways to find the element in which a given point is located, however one that has proved to be computationally efficient is the Barycentric Technique. This technique involves creating a parametrized coordinate system for a triangle (or any other given shape) so that it is relatively simple to find whether or not a point lies either on or within it. A detailed explanation of this technique can be found on pgs. 46-48 in [106]. The user simply supplies the beginning and ending points ((x_1, y_1) and (x_2, y_2)) of the desired interface and, by checking each element through an iterative loop, the Barycentric technique locates which element the beginning point lies in. The point, (x_1, y_1), is then used as $\mathbf{x}_s^e$ for this element, which allows for the solution of α. The time spent looping through each element to find where the point lies is relatively very short.

Box 3. Interface embedding algorithm.

Step 1: User-defined inputs of coordinates determining the beginning and terminating points, (x_1, y_1) and (x_2, y_2), of an interface (or interfaces) are read into the finite element code.

Step 2: In order to find the first element in which an interface will be embedded, the Barycentric technique is used to determine the element in which the point, (x_1, y_1), lies.

Step 3: For the first element, the point on the band in Equation 3.3.1, $\mathbf{x}_s^e$, is simply the user-defined input (x_1, y_1) and the interface orientation, $\boldsymbol{l}$, is calculated by finding the slope of the points (x_1, y_1) and (x_2, y_2). The orientation vector, $\boldsymbol{l}$, is stored and is assigned to all subsequent elements that lie between the points (x_1, y_1) and (x_2, y_2).

Step 4: The edge coordinates of the element are then found via Equation 3.3.1 and Equation 3.3.2.

Step 5: The adjacent elements are checked with the aid of an element neighbors array and interfaces are propagated through these elements, via steps 3 and 4 using each previous element's edge coordinate as $\mathbf{x}_s^e$. This is done until the terminal element is found.

Step 6: Store the band points and normals for each element that contains an interface in an array which will later be used for localization detection, and exit.

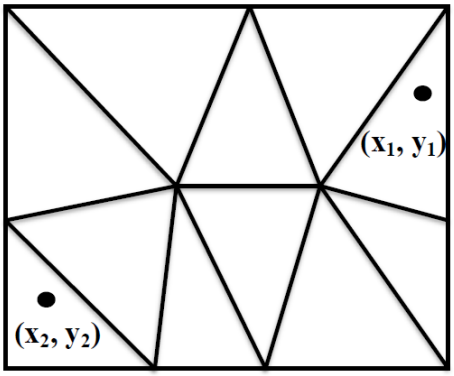

Figure 44: An interface which spans multiple elements begins and ends in the elements which fall within and in between the user-defined points (x_1, y_1) and (x_2, y_2).

3.4 Yield Criteria

The yield condition is based on the post-localization model in Section 2.4 and takes specific forms based on whether the band is compression or tension, hence

$$\Phi_{\text{compression}} = 0 = |\tau| - f - c_0 \tag{3.4.1}$$

$$\Phi_{\text{tension}} = 0 = \sqrt{(\tau)^2 + (\alpha_\sigma \langle\sigma\rangle)^2} - c_0 \tag{3.4.2}$$

where c_0 is the initial cohesion on the interface. The interface can also have a differing friction coefficient value, μ, from that of the bulk as well as differing values for α_ζ and α_σ. These differences reflect the fact that interfaces are often times governed by different fracture energies

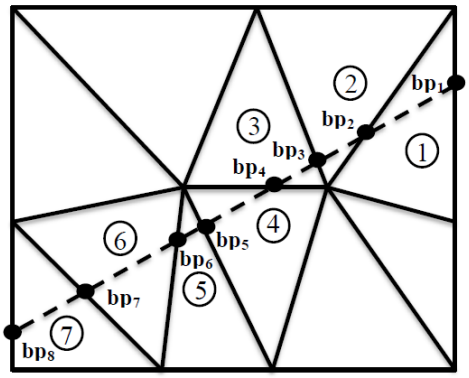

Figure 45: The algorithm in Box 3 initiates and propagates the band across the mesh in a continuous fashion until the terminal element is found.

than the bulk material. Also the interface may have its own unique surface topology, which is reflected in the friction coefficient.

Bulk localization is still captured in the manner described in Chapter 2 (see Section 2.2.2), through the use of the acoustic tensor. In elements with an interface, both the bulk and interface are examined, and the first criteria met is taken for the surface propagation. Therefore, fractures may propagate both through the bulk and along existing interfaces. There is then the possibility, as is the case for some masonry failure modes, of a crack originating in and propagating through the bulk, then traveling through a preexisting interface, and finally back into the bulk (Figure 47).

In the unlikely scenario in which, for a particular element, localization is detected in both the bulk and the interface in the same time step, the following equation is used to determine which one is more critical:

$$\min\left(\frac{\det\left(\boldsymbol{A}\right)}{\det\left(\boldsymbol{A}^{e}\right)},\ -\left(\frac{\Phi^{\text{trial}}}{||\boldsymbol{t}^{\text{crit}}||}\right)^{3}\right) \tag{3.4.3}$$

where $\boldsymbol{A}^{e}$ is the elastic acoustic tensor and $\boldsymbol{t}^{\text{crit}}$ is the critical traction necessary to cause yielding along the interface. Figure 47 depicts a situation commonly encountered in masonry problems, where a crack path travels through the bulk and briefly runs through a predefined interface and back into the bulk. The element with the interface may have also detected bulk localization, but since interfaces are usually weaker, the crack opted to take that path instead. However, there are instances in which the bulk may be weaker, especially if the material in question has a relatively low tensile strength and is subsequently subjected to a high tensile load.

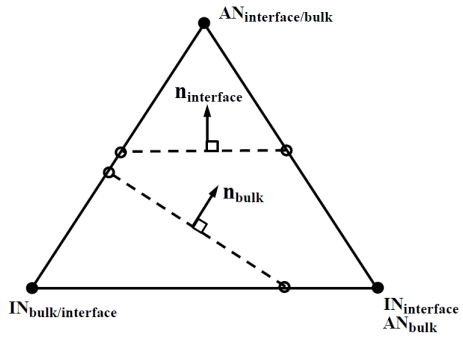

Figure 46: Element with predefined interface and possible bulk localization. The active and inactive nodes for each separate discontinuity surface may differ, which will affect the global crack path and its propagation.

To summarize, the mechanics on the surface of an interface are governed by the cohesive formulation in Section 2.4 and subsequently employs the same slip solving algorithms as well as the same finite element stiffness formulation detailed in Section 2.6, though the material properties may differ.

The algorithm with both preexisting and potential bulk interfaces is summarized in Box 4.

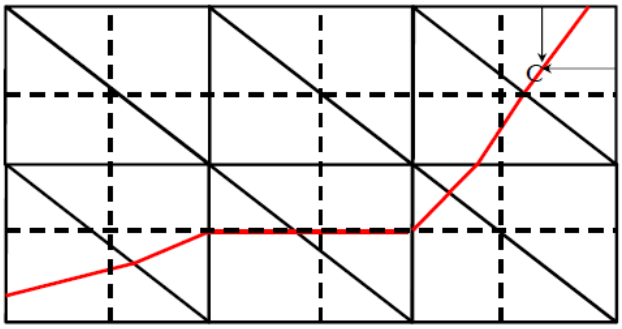

Figure 47: Example of a mesh with both vertical and horizontal preexisting interfaces. A given crack is detected first in the bulk (upper right element) and eventually propagates through an interface and back into the bulk material.

Box 4. Localization detection and band tracking algorithm for element w/ interface and bulk.

Step 1: For the interface, check the traction condition in either Equation 3.4.1 or Equation 3.4.2 and for the bulk, check for localization through the determinant of the acoustic tensor (Equation 2.2.8).

Step 2: If localization is detected in both within the same time step, then use Equation 3.4.3 to determine which one is more critical.

Step 2a: If the interface is more critical, use its stored band points and normal direction to the surface to find the edge coordinates, calculate the initial cohesion and find neighbor elements. Then, check adjacent elements for localization.

Step 2b: If the bulk is more critical, use the normal and slip direction determined from the acoustic tensor, find edge coordinates and also check adjacent elements for localization.

Step 3: Loop until all elements are checked, then exit when done.

3.5 Numerical Examples

Masonry is an excellent example of a material that may fail along an interface or through bulk material. The following examples are masonry focused and the material parameters are derived from earthen materials detailed in [107] and fit to a standard Drucker-Prager plasticity model. This model is able to capture the effects of friction, dilitancy (volumetric expansion), and material hardening which often occur in soil-based and geological materials. The model not only has a yield function to detect the inception of plasticity, but also what is known as

a plastic potential function which is employed to adjust the volumetric expansion. The yield and potential functions are distinct from each other, in what is known as a non-associative relationship. This affords the model the ability to eventually detect a bifurcation or fracture within the material (as described in Section 2.2.2).

Through the following examples, we demonstrate that the common failure patterns of masonry, e.g. splitting failure along headjoints, debonding along bedjoints and diffuse failure through the bulk, as catalogued in [18], are achievable using the aforementioned interface technology and post-localization model.

3.5.1 Two brick sliding test

TABLE IV: MATERIAL PARAMETERS FOR BRICK-MORTAR MASONRY W/ INTERFACES

Parameter	Symbol	Value
Young's Modulus	E	2800 MPa
Poisson's Ratio	ν	0.14
Cohesive Strength Parameter	α	0.80582 MPa
Friction Parameter	β	0.9251
Dilation Parameter	b	0.4626
Hardening Modulus	H	0.0 MPa
Localized Friction Coefficient	μ	0.7
Characteristic Slip Distance	ζ^*	0.3 mm
Normal Slip Coefficient	α_ζ	1.14
Normal Traction Coefficient	α_σ	1.14
Initial Interface Cohesion	c_0	0.42 MPa

The two-brick sliding test, a common test for measuring shear bond strength in masonry. In this simulation, the test is modeled using CST elements for both brick and mortar, and as Figure 49 depicts, interfaces are placed within the mortar element section close to the brick boundary. The confining displacement allows for a mode of pure shear. Material properties for this simulation are listed in Table IV. The deformed mesh (Figure 50) shows debonding at the bottom brick-mortar interface layer. The force-displacement graph reveals softening on the interface and eventually a complete degradation of the cohesive force.

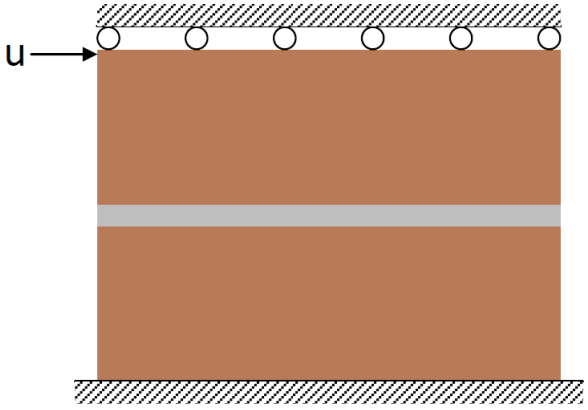

Figure 48: A simple setup of mortar sandwiched between two bricks. A confining displacement is placed on top to prevent rotation and the masonry unit is subjected to a shear displacement.

3.5.2 Masonry three-point bending test

This example is a masonry wall subjected to a three-point bending test. The interfaces are propagated in such a way that there are distinct areas for headjoints and as well as long, running

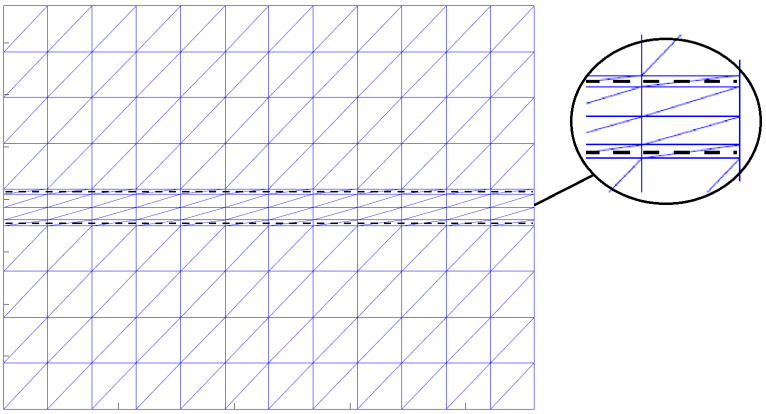

Figure 49: The interfaces are placed within the mortar elements near the boundary of the top and bottom bricks.

bedjoints (red lines). Three different refinements for this example was made and the softening responses are compared in Figure 58. In what comports with results in other numerical studies which simulate three-point bending tests [34, 108], the major path for the cracks is along the headjoints and collaterally along the bedjoints, though cracking and localization is also observed in the brick or bulk. Fracture traveling through the brick is somewhat more common for earthen masonry structures given that the brick and mortar are often of comparable strengths. This is in contrast to the more common clay fired bricks, which employ very weak mortar compared to the brick.

The softening response of the structures are plotted against the maximum crack mouth opening displacement (CMOD) observed at the bottom of the structure, the initiation of the major crack. High localization is shown along the headjoints and some zig-zagging can be seen taking a headjoint-bedjoint-headjoint path, particularly in Figure 54. The softening response of the

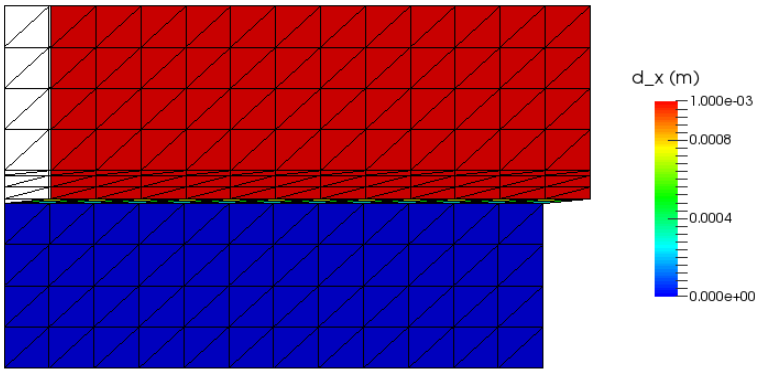

Figure 50: The deformed shape shows debonding along the bottom surface of the brick-mortar interface. The wire mesh in the background is the initial undeformed shape.

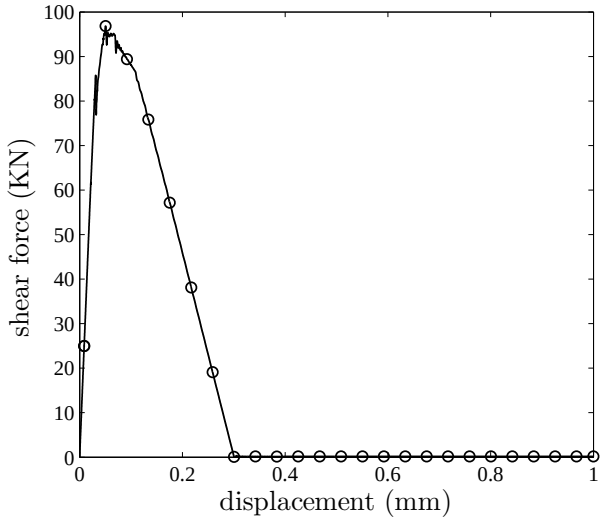

Figure 51: A characteristic degradation of the cohesion along the interface can be seen which eventually leads to a state of pure sliding.

finest mesh is the quickest and nearly predicts the lowest peak load. This is due to the fact that bebonding along the initial headjoint is captured with more accuracy than the coarser meshes. Namely, debonding along the interfaces in the middle of the specimen are displayed. However the crack paths in our simulation differs somewhat given that we use a mortar strength which is comparable to that of the brick (whereas the aforementioned studies use a very weak mortar), hence the fracture is prone to travel not only through the mortar and interfaces but, additionally, through the brick material as well.

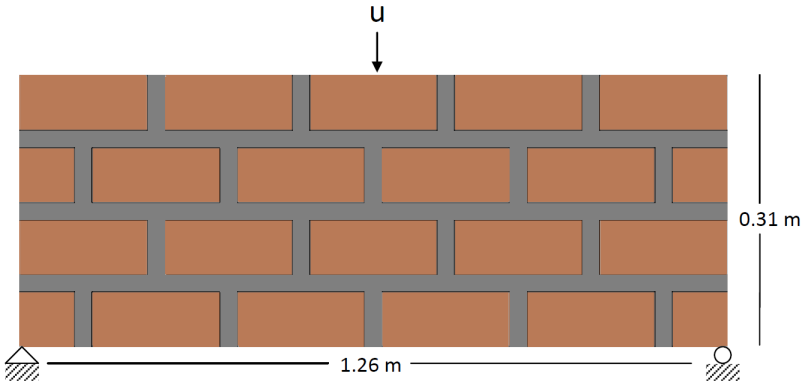

Figure 52: The specimen is completely constrained at the bottom left corner and is on a roller support on the bottom right, preventing translation in the vertical direction. It is subjected to a quasi-static downward displacement.

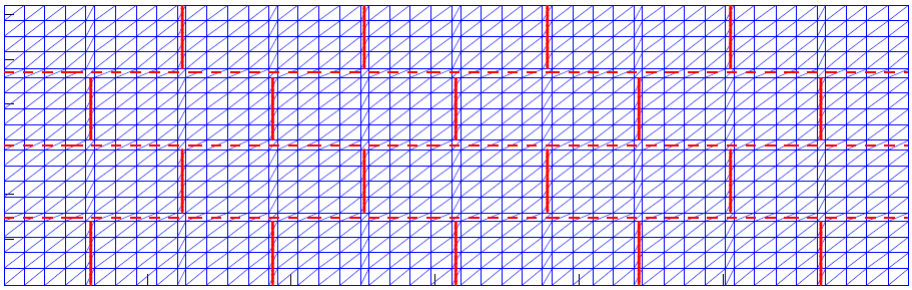

Figure 53: Brickwork mesh for three-point bending test. The interfaces are inserted at the midpoints of the mortar headjoints and bedjoints.

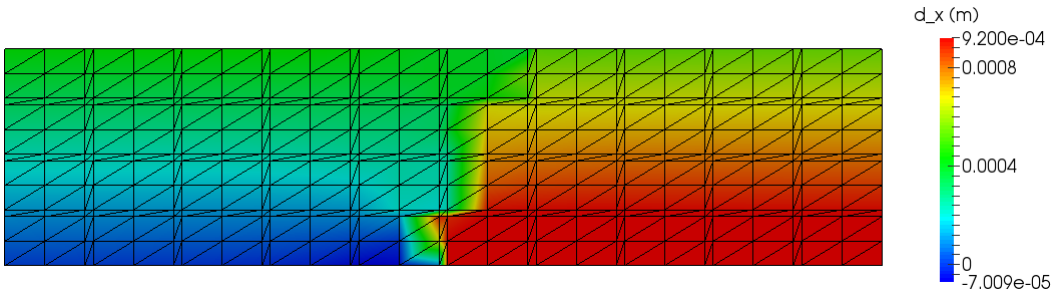

Figure 54: For the coarse mesh, a staircase pattern is observed where the structure debonds along the interfaces as well as through the bulk.

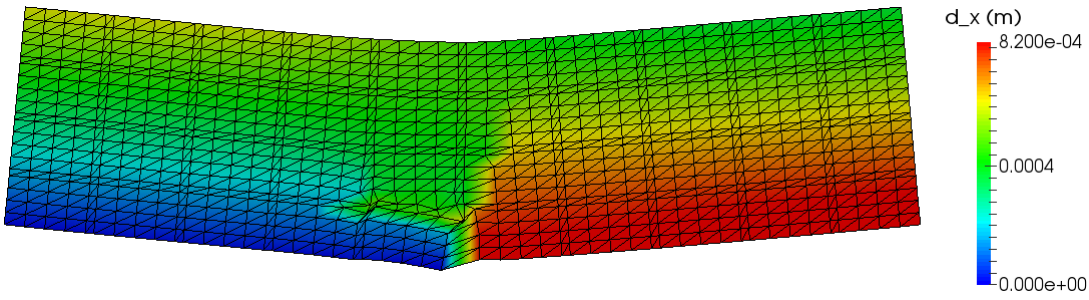

Figure 55: Significant deformation can be seen at the crack mouth opening, with collateral debonding along adjacent bedjoints.

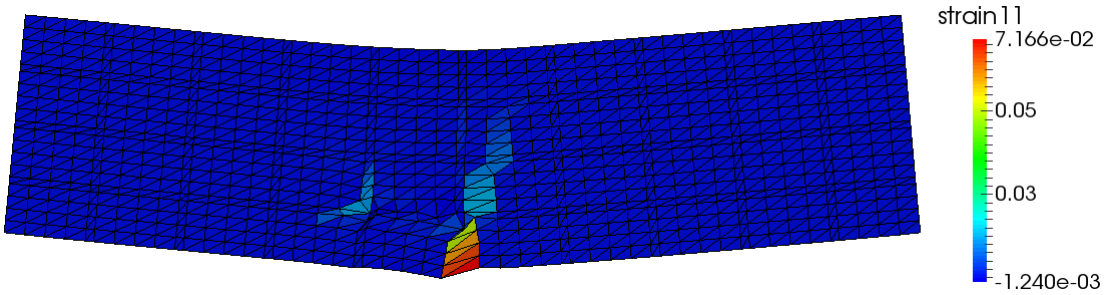

Figure 56: Strain localization is observed at the crack mouth opening.

3.5.3 Masonry wall w/hole

In a larger scale example, a masonry structure with a hole is simulated. It is confined at the top in the vertical direction in order to prevent rotation and sheared from the left side at the top. Full constraints are placed at the bottom to prevent translation.

Noticeably, as the cracks propagate along the interfaces, some of the bulk material can be seen rotating Figure 61. This occurs because both headjoints and bedjoints are debonding around a given brick. Also, some localization occurs within the bulk material and again a characteristic staircase pattern is observed near the corners of the opening (as in [34]), which experience high stress concentrations. The force-displacement graphs show softening within the macroscopic structure which indicates catastrophic failure.

3.6 Conclusions

The interface technology in this chapter is represented by a surface inserted into a continuum CST element. The concept of the strong discontinuity is utilized as well as an enhanced strain

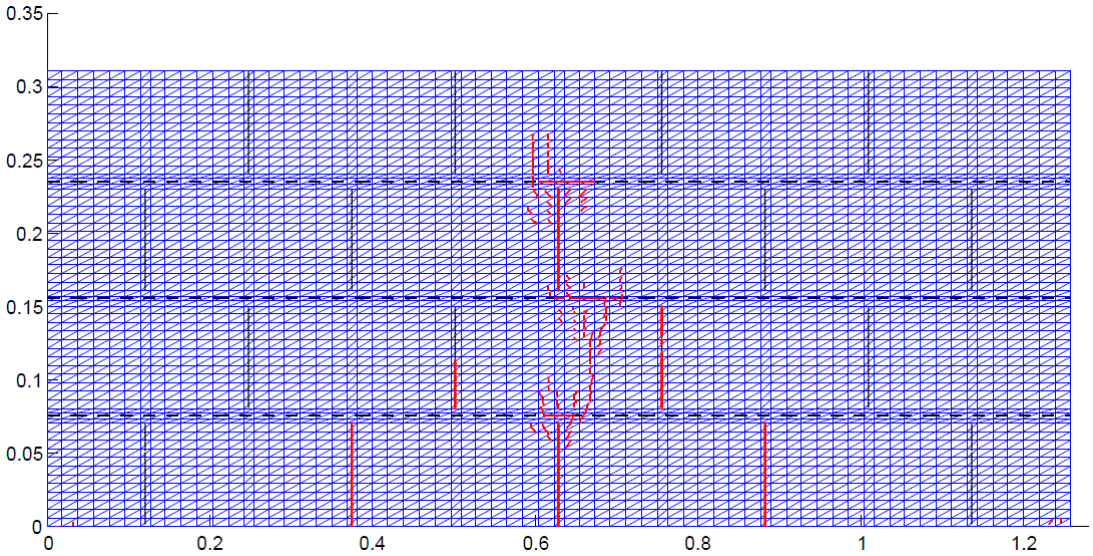

Figure 57: Crack path shows fracture along both head and bedjoints as well as through the bulk brick.

finite element. A methodology for propagating user-defined interfaces within a finite element mesh has been outlined. This method is particularly suited for structures such as periodic masonry, where interfaces between brick and mortar occur at regular intervals. The placement of these periodic interfaces can be easily algorithmized in order to propagate them at the desired locations. The deformation patterns of the masonry in this study show good agreement with prior studies which showcased these examples. A potential application for this methodology would be to validate experimental masonry results, featuring three-point bending tests and shear walls, which incorporate the use of brick and mortar. Experimental results do exist for masonry walls, constructed from earthen materials, subjected to flexure [107]. These are the focus of an upcoming study for the authors.

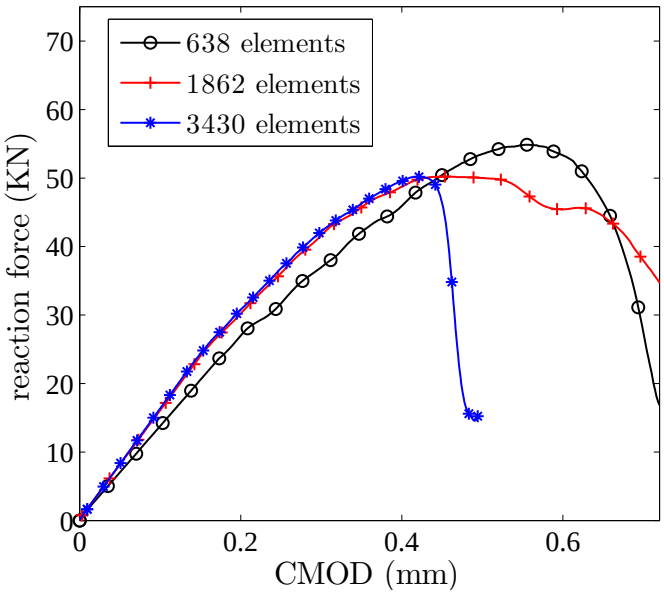

Figure 58: The force-displacement graphs reveal softening in the masonry specimen. The finest mesh shows a more abrupt history of softening than the other meshes.

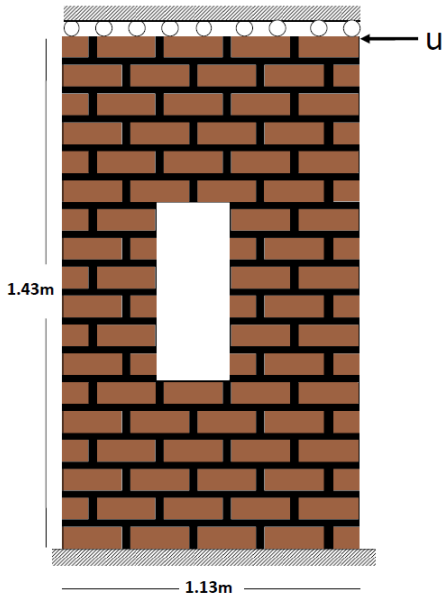

Figure 59: Boundary conditions for the wall subjected to pure shear. It is prevented from experiencing high rotation as well as translation on the bottom.

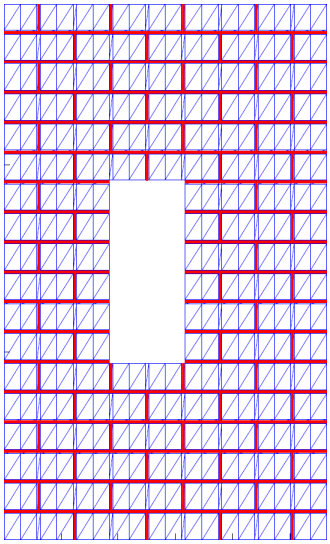

Figure 60: Headjoints and bedjoints are propagated in a characteristic masonry pattern.

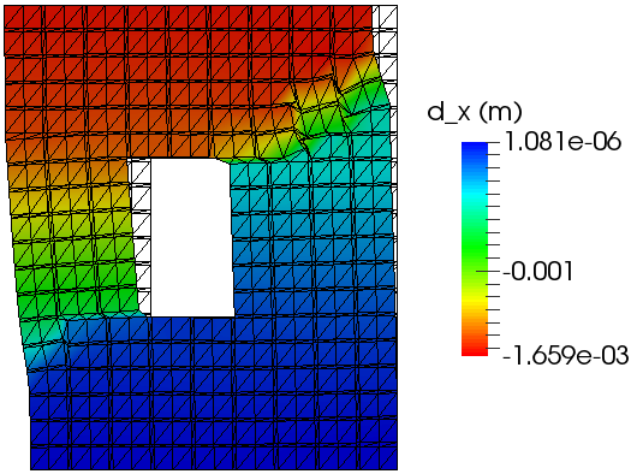

Figure 61: The deformed shape for the masonry wall in shear shows debonding along both headjoints and bedjoints as well as through the bulk material.

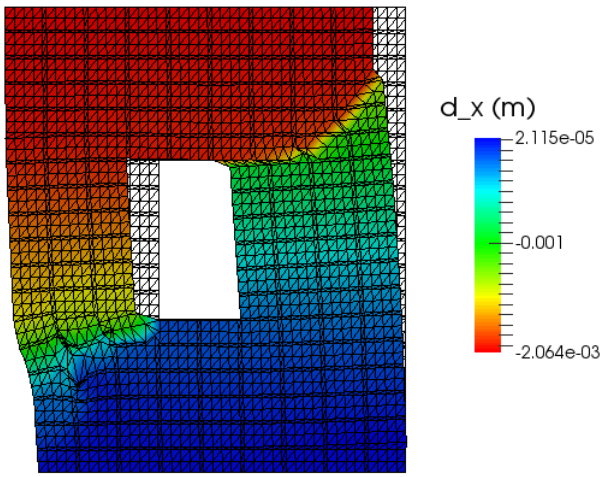

Figure 62: The refined view shows a sharp localization line in the bulk material and debonding of the brick-mortar interface at the top right and bottom left corners of the opening.

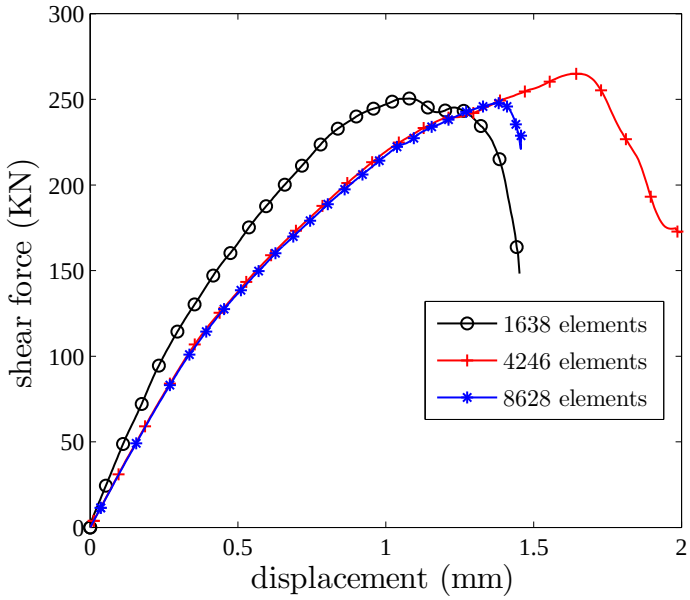

Figure 63: The coarsest mesh appears to over-predict the initial elastic response of the wall. The finest mesh predicts softening sooner than the 4246 element mesh suggesting that it captures debonding along the interfaces at an earlier point.

CHAPTER 4

APPLICATION OF ENHANCED STRAIN FINITE ELEMENTS TO RAMMED EARTH STRUCTURES

4.1 Introduction

Construction with soil-based materials is a practice that reaches back millennia. Typically soil needs to be either strengthened or stabilized to be useful in forming safe, durable structures. Material may be strengthened through mechanical compaction, baking or other means, or stabilized with additives such as cement, lime, and plant materials. Many techniques have been developed at different times and places.

While often considered primitive, modern engineers have begun reexamining these materials for reliability, economy and sustainability. Earthen materials tend to be highly sustainable, having low embodied energy and high thermal mass. Often the raw material can be sourced locally and, depending on the treatment, it can be recycled or returned to the soil when its service life is complete. In locations with relatively cheap labor and relatively high material costs, such structures are highly cost effective. Industrial techniques are being explored to bring labor costs down. Not to mention, comfortable and structurally sound dwellings can be built using earthen materials.

Soil may be used in several ways to create earthen structure. Soil block, also known as mud block, is compressed in a mechanical press to form a brick, and then cured. It is typically joined with standard or soil-cement mortar. Adobe is also a brick, but is sun baked. Cob wall is often built in place and has straw of other fibers for strength and ductility. In this chapter, we will focus on rammed earth, which is often stabilized with cement but compacted in place using forms to create the final structure.

Research into improving strength and durability has increased in the past two decades as well. Better proportioning of soil constituents and studies on optimum content of cement and other stabilizers [7, 109, 110] have improved performance.

Less is known about structural performance of elements. Some tests have been done of wall segments [111, 112]. Recently, some work has been done examining the strength and stiffness imparted by out-out-plane bending of walls [107, 113].

This work examines in-plane shear behavior and cracking of a cement-stabilized rammed earth wall. Rammed earth is a complex mixture of sand, clay and other fine soil particles, water, and cement. The behavior is quite complex, and we borrow a model for porous geomaterials to describe the behavior. While theoretically monolithic, rammed earth has weak interfaces between the compacted layers. In shear, a wall often, though not always, fails along these interfaces. To model the shear failure in the wall, we need account for both the possibility of failure along the weak interfaces as well as in the bulk material.

To model this, we propose to use an enhanced strain finite element, initially developed by Simo and coworkers [1]. This framework has been extended by many researchers, e.g. [55, 57, 58, 62, 114, 115] to examine various problems in fracture propagation. The standard finite element technology handles complex material models well, but not fracture and other localized failure methods. The enhancement allows a failure surface to be inserted when a critical condition is reached, at the critical orientation dictated by the condition. In this case, we used a classical bifurcation criterion, which detects the possibility of a jump in the strain or displacement field with no jump in the stress field. Once, the surface has been inserted, extra degrees of freedom control the slip along that surface, often using a traction-displacement law to govern the softening.

We extend the enhanced strain element to include the possibility to slip along a preexisting weak interface as well as the bulk materials. The model is then applied to the shear behavior of a structural wall.

4.2 Stabilized Rammed Earth Material Model

As mentioned previously, geomaterials have a very complex material behavior. To capture this behavior, we use a modified version of the Sandia GeoModel [90, 116–118].

Geomaterials are typically much weaker in tension than compression and have a nonlinear shear strength dependence. The GeoModel captures this with a combined linear-exponential shear failure surface F_f, defined by

$$F_f\left(I_1\right) = A - C\exp\left(B\,I_1\right) - \theta I_1 \tag{4.2.1}$$

and shown in Figure 64. The initial yield surface is offset from the failure surface by a constant parameter N. Although not particularly important for this application, under high mean stresses inelastic compactive deformation can occur due to pore collapse, grain crushing, and other phenomena. Hence an elliptical cap is added to model this type of deformation. The elliptical shape allow compactive and shear inelasticity to interact over a range of pressures. Recently [90], an elliptical tension cap was also added to the model to better capture the tensile strength. The modified cap function for the compressive and tensile caps becomes

$$F_c\left(I_1,\kappa\right) = 1 - H\left(\kappa - I_1\right)\left(\frac{I_1-\kappa}{X\left(\kappa\right)-\kappa}\right)^2 - H\left(I_1 - I_1^T\right)\left(\frac{I_1 - I_1^T}{3T - I_1^T}\right)^2 \tag{4.2.2}$$

Finally, the yield surface is adjusted using a third-invariant modifying function of the Gudehus [117, 119] type, to capture the different between triaxial extension and compression strength inherent in geomaterials. This function has the form

$$\Gamma(\beta^\xi) = \frac{1}{2}\left[1 + \sin\left(3\beta^\xi\right) + \frac{1}{\psi}\left(1 - \sin\left(3\beta^\xi\right)\right)\right] \tag{4.2.3}$$

where ψ is the ratio of triaxial extension to compression strength and θ is the Lode angle.

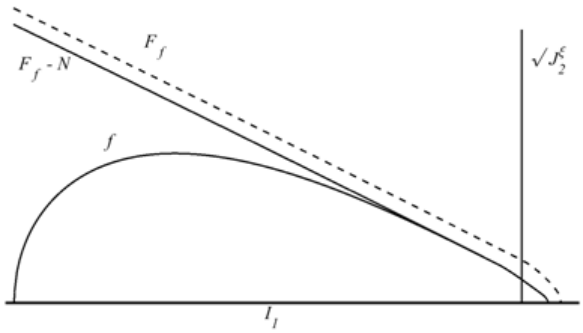

Figure 64: Pressure-dependent yield function f for GeoModel in Meriodional stress space, showing shear failure surface F_f, and shear yield surface $F_f - N$

Inelastic hardening of yield surface is of two types. The shear yield surface undergoes kinematic hardening to capture the Bauschinger effect under cyclic loading. The cap surface, on the other hand, experiences isotropic hardening, strengthening as the material compresses. The motion and growth of the yield surface is shown in Figure 65.

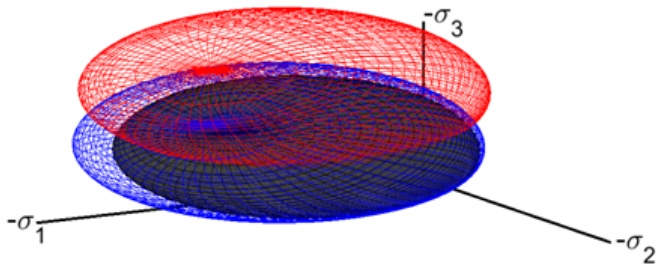

Figure 65: Evolution of the yield surface in principal stress space, showing growth from the initial (black) yield surface to growth from isotropic hardening (blue) and translation due to kinematic hardening (red).

For more details of the governing equations and numerical implementation of the model, the reader is referred to [90].

4.3 Fracture Model

The bifurcation condition of Rudnicki and Rice, 1975 is used to mark the onset of localization. This condition was based of earlier work of Hill [83] and others. This criterion was examined and applied to the GeoModel in [101]. This condition says that when the acoustic tensor loses its positive definite character a localized band or surface can form. The acoustic tensor $\boldsymbol{A}$ is defined as

$$\boldsymbol{A}(\boldsymbol{n}) = \boldsymbol{n} \cdot \boldsymbol{C} \cdot \boldsymbol{n} \tag{4.3.1}$$

where $\boldsymbol{C}$ is either the elastoplastic or the elastic-perfectly plastic modulus, depending whether a weak discontinuity (jump in the strain field) or strong discontinuity (jump in the displacement field) is being tested. The normal to the surface $\boldsymbol{n}$ is part of the equation, and hence a search must be conducted for the critical normal. Once found, however, the orientation of the failure surface is known.

Once localization is detected, a failure surface is inserted into the finite element in which the localization occurred. The orientation is the most critical determined by the bifurcation, while the position is in line with the propagating band. For the first element of a band, the band passes through the centroid of the element.

A traction-displacement relationship in the spirit of damage mechanics governs the softening on the localized surface. This relationship is described in detail in [62]. Separate yield strengths in tension and pure shear are given, and in the mixed mode case an elliptical relationship couples the two. This strength degrades linearly with displacement on the band, but maintains a constant ratio. A different ratio may govern the slip, such that normal and shear stiffnesses are unequal, but again, these maintain a constant ratio as the material degrades. The material unloads and reloads toward the origin.

For existing weak interfaces, in this case between compacted layers, an initial yield strength is given on the band. This is of the same form as above, but with different material properties, as such interfaces are typically weaker than a bulk material.

These constitutive models are incorporated into an enhanced strain finite element. This framework, originally proposed in [1] has been extended by many researchers, for example [54, 57, 58, 114, 120]. The bulk constitutive model can be incorporated at the integration points in the standard way for as for any finite element analysis.

At the end of each time step, each element is checked for localization. The bifurcation condition is checked at the bulk integration points, while on any preexisting surfaces, the yield condition is checked. In the rare case that both criteria are present, a check is made to determine which is more critical. A surface is inserted at the critical orientation and location.

In subsequent time steps, the traction-displacement equations are solved to determine the relative motion of the surfaces on the band, along with the continuum deformation. Because

of the piecewise constant nature of the slip on the band in the enhanced strain method, the extra degrees of freedom related to the jump on the fracture surface may be condensed out at the element level. Hence, the global finite element code needs no knowledge of the extra degrees of freedom, and the element can be inserted into a global finite element code with little modification.

4.4 Numerical Example

As an example, we examine the shear behavior of a rammed earth wall with openings. The geometry is shown in Figure 66. The wall has openings for a door and a window. For simplicity, we have inserted two interfaces, representing weak areas between the layers, at the top of the door and at midheight. A real wall may have more layers. For comparison, we run a similar model assuming there are no weak interfaces. A shear displacement, representing a strong wind force, is applied from the left, to a maximum displacement of 10 cm at the top.

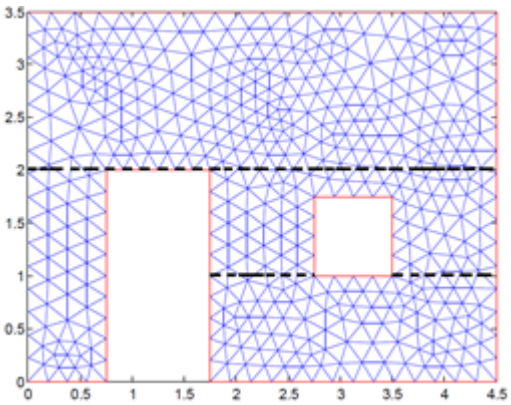

Figure 66: Mesh of a wall of an earthen structure with weak interfaces. Distances are in meters.

The bulk properties of the wall are adapted from a Gosford sandstone test, as they have similar compositions. These properties are listed in Table V.

TABLE V: MATERIAL PARAMETERS FOR BULK MATERIAL

Parameter	Symbol	Value
Young's Modulus	E	31772.4 MPa
Poisson's Ratio	ν	0.1286
Isotropic Tensile Strength	T	15 MPa
Tension cap parameter	I_1^T	0.0 MPa
Shear yield surface parameter	A	1255.7 MPa
Shear yield surface parameter	B	1.93e-4 1/MPa
Shear yield surface parameter	C	1248.2 MPa
Shear yield surface parameter	θ	0.0 rad
Potential surface parameter	L	1255.7 1/MPa
Potential surface parameter	ϕ	0.0 rad
Compression cap parameter	κ_0	10.7 MPa
Aspect ratios for compression cap	R,Q	18.5
Isotropic hardening parameter	W	0.1536
Isotropic hardening parameter	D_1	9.283e-4 1/MPa
Isotropic hardening parameter	D_1	0.0
Kinematic hardening parameter	c_α	0.05 MPa
Kinematic hardening parameter	N	1.0 MPa
Stress triaxiality parameter	ψ	1.0

The localized parameters for the bulk and preexisting interfaces are shown in Table VI.

The displaced shapes are shown in Figure 67, and the fractured elements in Figure 68. The major slip surfaces are colored in red. As can be seen, a more dominant failure line and more localized failure occur when there are weak interfaces. Some of the fracture propagates

TABLE VI: MATERIAL PARAMETERS FOR BULK AND PREEXISTING INTERFACES

Parameter	Symbol	Value
Bulk Interfaces		
Localized Friction Coefficient	μ	0.7
Characteristic Slip Distance	ζ^*	0.5 mm
Normal Slip Coefficient	α_ζ	1.14
Normal Traction Coefficient	α_σ	1.14
Preexisting Interfaces		
Localized Friction Coefficient	μ	0.7
Characteristic Slip Distance	ζ^*	0.5 mm
Normal Slip Coefficient	α_ζ	1.0
Normal Traction Coefficient	α_σ	1.0
Initial Interface Cohesion	c_0	0.42 MPa

through the bulk material even when weak interfaces are present, however, indicating that both mechanisms are important.

The force displacement curve is shown in Figure 69.

4.5 Conclusions

In summary, we have developed a finite element model for analyzing earthen structural materials. The model includes plasticity of the bulk material, localization, and propagating fractures both on existing weak interfaces and in the bulk material.

Preliminary examples show that the weak interfaces tend to decrease ductility and distribution of damage. They also tend to decrease overall strength in the wall. For shear design, special considerations should be made to detail interfaces between layers to increase their strength.

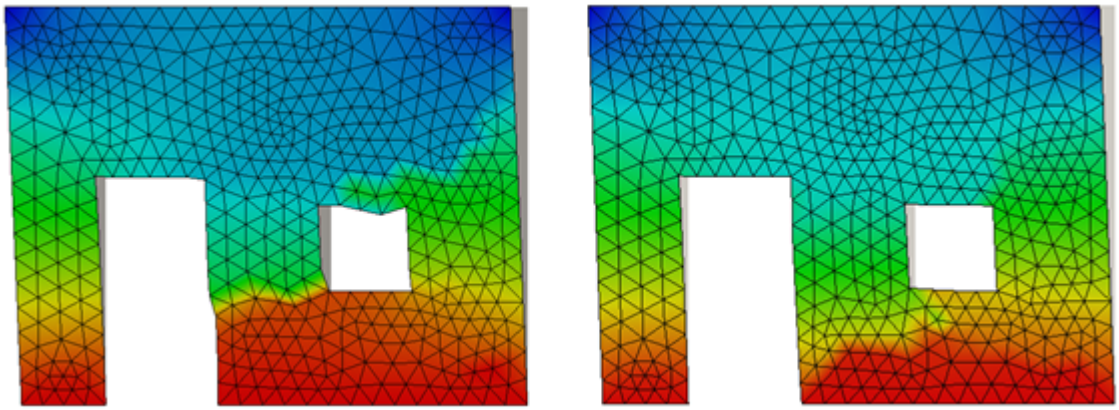

Figure 67: Deformed shape of walls with weak interfaces (left side) and without (right side). The weak interfaces show less homogeneous deformation change due to fewer fractures. Maximum displacement is 10 cm in each case.

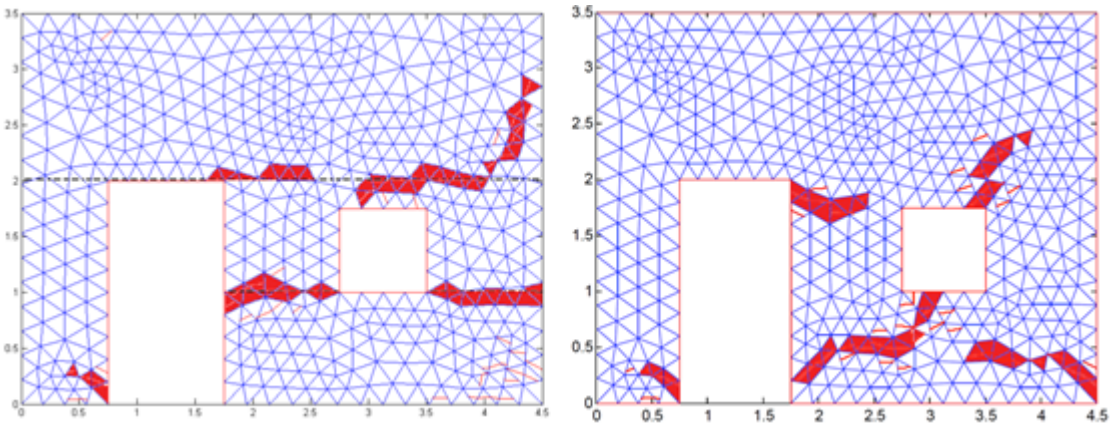

Figure 68: Fractured elements (thin red lines) and major fractures in the material. Left side is with weak interfaces, and right side without.

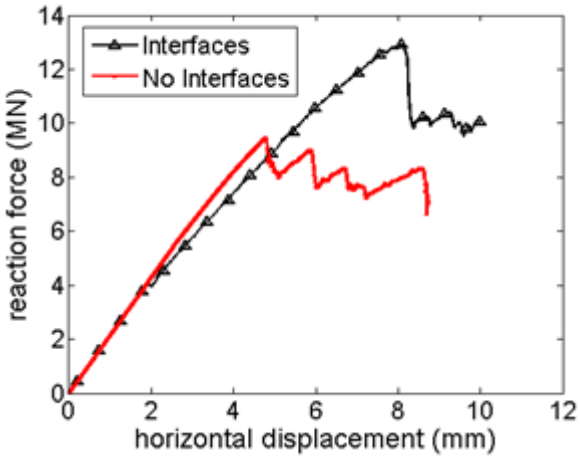

Figure 69: Force-displacement curve of wall with and without weak interfaces.

Further testing is necessary to more accurately determine material properties, especially of the interfaces. Then the effects of interfaces and geometric design can be better quantified.

CHAPTER 5

CONCLUSIONS AND FUTURE WORK

5.1 Conclusions

This dissertation presents a framework for capturing and tracking failure patterns in earthen structures. Within a finite element context, the following have been implemented: a criterion for predicting the inception of failure, a novel post-localization constitutive model for describing the evolution of fracture along a crack surface, and a method for embedding preexisting interfaces within a given material. These components are cast in the framework of embedded strong discontinuities coupled with an enhanced strain element which is suited for regularizing the unbounded strain field for elements which experience localized softening.

Over the years, the predominant failure mode of interest in geologically-based materials has focused on intense shearing and compaction. Recently, interest in materials such as earthen brick and rammed earth for usage in constructing living quarters has increasingly grown. These structures are not only subjected to shear and compression, but they also exhibit flexural behavior and splitting fractures due to tensile loads. Therefore, from a theoretical and numerical modeling standpoint, it is necessary to develop them such that they can handle mixed modes of failure. To this end, a novel traction-separation has been developed and presented in this thesis. In the tensile regime, the evolution of failure through a given material is governed by

an elliptical interaction between shear and normal tractions on the crack surface. In order to reproduce the behavior of the actual material, this interaction is informed by the experimental values of the energy release rate in Mode I (opening) and Mode II (sliding) failure regimes. In the compressive regime, failure evolution is governed by an interaction between the shear traction and the friction, which behaves in a plastic-like manner, upon the crack surface. The numerical examples show that spurious geometric locking seen in [57] is remedied by the added opening failure mode. For large-scale structures which exhibit complex interactions between failure modes, such as slope stability, material softening is successfully captured using the traction-separation model.

Additionally, finite element simulations which incorporate the use of embedded discontinuities are known to suffer from a lack of numerical robustness, i.e. that ability to stabilize itself as the simulation progresses and encounters solution difficulties. In this dissertation, a modified version of the Impl-Ex technique (see [52]) is incorporated which uses a combination of implicit and explicit integration schemes in order to increase simulation robustness. The numerical examples show that for a sufficiently small time step, the modified Impl-Ex method is able to reach the accuracy of a fully implicit integration scheme. This integration method allowed for the simulation of geometrically complex shapes which are prevalent, for instance, in earthen structures.

A new method for embedding predefined interfaces within a finite element mesh was also detailed and applied in this dissertation. Preexisting interfaces are a common of feature of many composite materials. Namely, for masonry structures, the interaction between the brick-mortar

interface is an inherent feature which affects the behavior of said structures in complex ways. An algorithm was designed and implemented, building off of the work of [57], which allows a user to specify the number of interfaces and their individual orientations within a finite element mesh. The algorithm locates the beginning and ending points of a given interface and proceeds to propagate it through neighboring elements. The softening mechanics on these interfaces are governed by the previously mentioned traction-separation model. In addition, the interfaces possess their own unique properties from that of the bulk, such as cohesive strength, friction coefficient, and energy release rates. The examples showed the applicability of the interface method through simulating periodic masonry structures. Failure was observed to occur along the interfaces and through the bulk material, common in many realistic masonry failure scenarios. Future studies hope to use material parameters from experimental studies in order to match the peak strengths and softening curves.

In the final chapter detailing modeling and simulations, a modified version of the Sandia Geomodel [90] was coupled with the traction-separation model and the interface embedding technology to simulate a rammed earth structure which possessed interfaces at the layers of compaction. It was demonstrated that the dominant mode of failure occurred along the interfaces, with some diffuse fracturing in the bulk material, which was expected. In future studies, the aim is to fit the modified Geomodel to the earthen structural materials found in [107, 113].

The framework for capturing and tracking failure patterns in earthen structures presented in this dissertation shows promise for modeling a diverse number of earthen structures. It is hoped that this framework will be able to reproduce failure seen in experiments detailed in, but not

limited to, [107] and [41]. While this dissertation presents a significant step in this direction, more work needs to be done in developing the model, which will be detailed in the next section.

5.2 Future Work

There exist a number of possible ways that this research can be taken forward. One instance is the type of element employed in this study. While the traction-separation model featured in this dissertation prevents spurious geometric locking to a great degree, the issues of solution accuracy remains. Constant strain triangles (CST) while a simple and effect finite element, are known to cause solutions to be overstiff and do not handle stress concentrations (e.g. stresses seen at the corners of holes) particularly well. Refinement may help, but even still the elements seem to negatively affect mesh-independence. One possible way to remedy this would be to incorporate formulations for quadrilateral elements as described in [121]. Another possible solution is to implement a six-noded triangle which, as a consequence of having more interpolation functions, is considerably more accurate than CST's. Also, an extension to three dimensions may be extremely useful, if not necessary, in modeling large-scale masonry structures. If, in this vein, an embedded discontinuity approach is still taken, then implementing the formulations in [120] would most likely be pursued.

Implementing a post-localization variable friction formulation is also a strong consideration for future models. It is known that geomaterials exhibit unstable friction slip upon faulting or cracking, therefore implementing an already established form like that of [57] is an attractive choice.

Lastly, while experimental data exists for earthen structural materials, it is hoped that stress-strain data and other parameters may be obtained for a number of these materials (as well as data from full-scale masonry tests). With this data, various materials could be fit to the modified Sandia Geomodel. And coupling this with the traction-separation model, a number of important structural problems involving earthen materials could be simulated and further investigated.

APPENDICES

Appendix A

DERIVATIVES OF THE YIELD FUNCTIONS

The gradients of the yield functions are as follows:

$$\frac{\partial \Phi_1}{\partial \zeta_n} = \frac{\partial \sigma}{\partial \zeta_n} - \left[\zeta_n \frac{\partial k_n}{\partial \zeta_n} + k_n\right] \tag{A.0.1}$$

$$\frac{\partial \Phi_1}{\partial \zeta_s} = \frac{\partial \sigma}{\partial \zeta_s} - \zeta_n \frac{\partial k_n}{\partial \zeta_s} \tag{A.0.2}$$

$$\frac{\partial \Phi_2}{\partial \zeta_n} = \frac{\partial \tau}{\partial \zeta_n} - \zeta_s \frac{\partial k_s}{\partial \zeta_n} \tag{A.0.3}$$

$$\frac{\partial \Phi_2}{\partial \zeta_s} = \frac{\partial \tau}{\partial \zeta_n} - \left[\zeta_s \frac{\partial k_s}{\partial \zeta_s} + k_s\right] \tag{A.0.4}$$

where

$$\frac{\partial k_s}{\partial \zeta_n} = \begin{cases} -\dfrac{\alpha_\zeta^2 c_0}{\zeta_c^3}\zeta_n & \texttt{if} \quad \zeta_{eq} = \zeta_c \\ 0 & \texttt{if} \quad \zeta_{eq} < \zeta_c \end{cases} \tag{A.0.5}$$

$$\frac{\partial k_s}{\partial \zeta_s} = \begin{cases} -\dfrac{c_0}{\zeta_c^3}\zeta_s & \texttt{if} \quad \zeta_{eq} = \zeta_c \\ 0 & \texttt{if} \quad \zeta_{eq} < \zeta_c \end{cases} \tag{A.0.6}$$

$$\frac{\partial k_n}{\partial \zeta_n} = \frac{\alpha_\zeta}{\alpha_\sigma}\frac{\partial k_s}{\partial \zeta_n} \tag{A.0.7}$$

$$\frac{\partial k_n}{\partial \zeta_s} = \frac{\alpha_\zeta}{\alpha_\sigma}\frac{\partial k_s}{\partial \zeta_s} \tag{A.0.8}$$

Appendix A (Continued)

To determine the derivatives of the bulk stresses with respect to the jumps, recall

$$\boldsymbol{\sigma}_{n+1} = \boldsymbol{\sigma}_n + \boldsymbol{c}^e : \Delta\boldsymbol{\epsilon}^{\text{conf}} - \boldsymbol{c}^e : \left(\Delta\boldsymbol{\zeta} \otimes \nabla f^h\right)^s \tag{A.0.9}$$

Hence,

$$\frac{\partial \boldsymbol{\sigma}}{\partial \boldsymbol{\zeta}_n} = -\boldsymbol{c}^e : \left(\boldsymbol{n} \otimes \nabla f^h\right)^s \tag{A.0.10}$$

$$\frac{\partial \boldsymbol{\sigma}}{\partial \boldsymbol{\zeta}_s} = -\boldsymbol{c}^e : \left(\boldsymbol{l} \otimes \nabla f^h\right)^s \tag{A.0.11}$$

and therefore

$$\frac{\partial \sigma}{\partial \boldsymbol{\zeta}_n} = -\left(\boldsymbol{n} \otimes \boldsymbol{n}\right) : \boldsymbol{c}^e : \left(\boldsymbol{n} \otimes \nabla f^h\right)^s \tag{A.0.12}$$

$$\frac{\partial \sigma}{\partial \boldsymbol{\zeta}_s} = -\left(\boldsymbol{n} \otimes \boldsymbol{n}\right) : \boldsymbol{c}^e : \left(\boldsymbol{l} \otimes \nabla f^h\right)^s \tag{A.0.13}$$

$$\frac{\partial \tau}{\partial \boldsymbol{\zeta}_n} = -\left(\boldsymbol{n} \otimes \boldsymbol{l}\right)^s : \boldsymbol{c}^e : \left(\boldsymbol{n} \otimes \nabla f^h\right)^s \tag{A.0.14}$$

$$\frac{\partial \tau}{\partial \boldsymbol{\zeta}_s} = -\left(\boldsymbol{n} \otimes \boldsymbol{l}\right)^s : \boldsymbol{c}^e : \left(\boldsymbol{l} \otimes \nabla f^h\right)^s \tag{A.0.15}$$

Appendix B

DERIVATION OF THE EFFECTIVE ALGORITHMIC OPERATOR

The effective algorithmic operator is defined as

$$\boldsymbol{C}_{n+1}^{\text{eff}} = \frac{\partial \tilde{\boldsymbol{\sigma}}_{n+1}}{\partial \boldsymbol{\epsilon}_{n+1}} \tag{B.0.1}$$

by taking the derivative of the semi-implicit stress in eq. (Equation 2.6.15) with respect to the implicit strain we have the following:

$$\begin{aligned}\frac{\partial \tilde{\boldsymbol{\sigma}}_{n+1}}{\partial \boldsymbol{\epsilon}_{n+1}} &= \frac{\partial \boldsymbol{\sigma}_n}{\partial \boldsymbol{\epsilon}_{n+1}} + \boldsymbol{c}^e : \frac{\partial \left(\boldsymbol{\epsilon}_{n+1} - \boldsymbol{\epsilon}_n\right)}{\partial \boldsymbol{\epsilon}_{n+1}} \\ &\quad - \Delta\tilde{\lambda}_{n+1}\boldsymbol{c}^e : \frac{\partial}{\partial \boldsymbol{\epsilon}_{n+1}}\left(\frac{\partial g\left(\tilde{\boldsymbol{\sigma}}_{n+1}\right)}{\partial \tilde{\boldsymbol{\sigma}}_{n+1}}\right) \\ &= \boldsymbol{c}^e : \frac{\partial \boldsymbol{\epsilon}_{n+1}}{\partial \boldsymbol{\epsilon}_{n+1}} - \Delta\tilde{\lambda}_{n+1}\boldsymbol{c}^e : \tilde{\boldsymbol{A}}_{n+1} : \frac{\partial \tilde{\boldsymbol{\sigma}}_{n+1}}{\partial \boldsymbol{\epsilon}_{n+1}}\end{aligned} \tag{B.0.2}$$

where

$$\tilde{\boldsymbol{A}}_{n+1} = \frac{\partial^2 g\left(\tilde{\boldsymbol{\sigma}}_{n+1}\right)}{\partial \tilde{\boldsymbol{\sigma}}_{n+1} \otimes \tilde{\boldsymbol{\sigma}}_{n+1}} \tag{B.0.3}$$

Appendix B (Continued)

Noting that $\boldsymbol{c}^e : \frac{\partial \boldsymbol{\epsilon}_{n+1}}{\partial \boldsymbol{\epsilon}_{n+1}} = \boldsymbol{c}^e : \boldsymbol{I} = \boldsymbol{c}^e$, we group terms and factor:

$$\frac{\partial \tilde{\boldsymbol{\sigma}}_{n+1}}{\partial \boldsymbol{\epsilon}_{n+1}} = \boldsymbol{c}^e - \Delta\tilde{\lambda}_{n+1}\boldsymbol{c}^e : \tilde{\boldsymbol{A}}_{n+1} : \frac{\partial \tilde{\boldsymbol{\sigma}}_{n+1}}{\partial \boldsymbol{\epsilon}_{n+1}}$$

$$\boldsymbol{c}^e = \frac{\partial \tilde{\boldsymbol{\sigma}}_{n+1}}{\partial \boldsymbol{\epsilon}_{n+1}} + \Delta\tilde{\lambda}_{n+1}\boldsymbol{c}^e : \tilde{\boldsymbol{A}}_{n+1} : \frac{\partial \tilde{\boldsymbol{\sigma}}_{n+1}}{\partial \boldsymbol{\epsilon}_{n+1}}$$

$$\boldsymbol{c}^e = \left(\boldsymbol{I} + \Delta\tilde{\lambda}_{n+1}\boldsymbol{c}^e : \tilde{\boldsymbol{A}}_{n+1}\right) : \frac{\partial \tilde{\boldsymbol{\sigma}}_{n+1}}{\partial \boldsymbol{\epsilon}_{n+1}}$$

finally

$$\frac{\partial \tilde{\boldsymbol{\sigma}}_{n+1}}{\partial \boldsymbol{\epsilon}_{n+1}} = \left(\boldsymbol{I} + \Delta\tilde{\lambda}_{n+1}\boldsymbol{c}^e : \tilde{\boldsymbol{A}}_{n+1}\right)^{-1} : \boldsymbol{c}^e = \boldsymbol{C}^{\text{eff}}_{n+1} \tag{B.0.4}$$

CITED LITERATURE

Bibliography

[1] Simo, J. C., Oliver, J., and Armero, F.: An analysis of strong discontinuities induced by strain-softening in rate-independent inelastic solids. Computational Mechanics, 12(5):277–296, 1993.

[2] Oliver, J., Huespe, A. E., and Samaniego, E.: A study on finite elements for capturing strong discontinuities. International Journal for Numerical Methods in Engineering, 56(14):2135–2161, 2003.

[3] Reddy, B. V. V., Lal, R., and Rao, K. S. N.: Influence of joint thickness and mortar-block elastic properties on the strength and stresses developed in soil-cement block masonry. Journal of Materials in Civil Engineering, 21(10):535–542, 2009.

[4] Rao, K. V. M., Reddy, B. V., and Jagadish, K.: Flexural bond strength of masonry using various blocks and mortars. Materials and Structures, 29(2):119–124, 03/21 1996. M3: 10.1007/BF02486202.

[5] Walker, P. and Stace, T.: Properties of some cement stabilised compressed earth blocks and mortars. Materials and Structures, 30(9):545–551, 11/21 1997. M3: 10.1007/BF02486398.

[6] Walker, P.: Bond characteristics of earth block masonry. Journal of Materials in Civil Engineering, 11(3):249–256, August 1999 1999.

[7] Reddy, B. V. and Walker, P.: Stabilised mud blocks : Problems, prospects. In EarthBuild 2005 Conference, pages 63–75, Sydney, Australia. UTS.

[8] Reddy, B. V. V. and Gupta, A.: Strength and elastic properties of stabilized mud block masonry using cement-soil mortars. Journal of Materials in Civil Engineering, 18(3):472–476, May/June 2006 2006.

[9] Reddy, B. V. V. and Gupta, A.: Tensile bond strength of soil-cement block masonry couplets using cement-soil mortars. Journal of Materials in Civil Engineering, 18(1):36–45, January/February 2006 2006.

[10] Reddy, B. V. V., Lal, R., and Rao, K. S. N.: Optimum soil grading for the soil-cement blocks. Journal of Materials in Civil Engineering, 19(2):139–148, February 2007 2007.

[11] Venkatarama Reddy, B. and Uday Vyas, C.: Influence of shear bond strength on compressive strength and stress–strain characteristics of masonry. Materials and Structures, 41(10):1697–1712, 12 2008.

[12] Burroughs, S.: Soil property criteria for rammed earth stabilization. Journal of Materials in Civil Engineering, 20(3):264–273, 2008.

Appendix B (Continued)

[13] Maniatidis, V. and Walker, P.: Structural capacity of rammed earth in compression. Journal of Materials in Civil Engineering, 20(3):230–238, 2008.

[14] Jaquin, P., Augarde, C., Gallipoli, D., and Toll, D.: The strength of unstabilised rammed earth materials. Géotechnique., 59(5):487–490, 2009.

[15] Ciancio, D. and Gibbings, J.: Experimental investigation on the compressive strength of cored and molded cement-stabilized rammed earth samples. Construction and Building Materials, 28(1):294–304, 2012.

[16] Ciancio, D., Jaquin, P., and Walker, P.: Advances on the assessment of soil suitability for rammed earth. Construction and Building Materials, 42:40–47, 2013.

[17] Ciancio, D., Beckett, C., and Carraro, J.: Optimum lime content identification for lime-stabilised rammed earth. Construction and Building Materials, 53:59–65, 2014.

[18] Andreaus, U.: Failure criteria for masonry panels under in-plane loading. Journal of Structural Engineering, 122(1):37–46, 1996.

[19] Rots, J. G.: Computational modeling of concrete fracture. Doctoral dissertation, Technische Hogeschool Delft, 1988.

[20] Lourenco, P. B. and Rots, J. G.: Multisurface interface model for analysis of masonry structures. Journal of engineering mechanics, 123(7):660–668, 1997.

[21] Lotfi, H. and Shing, P.: An appraisal of smeared crack models for masonry shear wall analysis. Computers & Structures, 41(3):413 – 425, 1991.

[22] Giambanco, G. and Gati, L. D.: A cohesive interface model for the structural mechanics of block masonry. Mechanics Research Communications, 24(5):503 – 512, 1997.

[23] Giambanco, G., Rizzo, S., and Spallino, R.: Numerical analysis of masonry structures via interface models. Computer methods in applied mechanics and engineering, 190(49-50):6493–6511, 2001.

[24] Alfano, G. and Crisfield, M.: Finite element interface models for the delamination analysis of laminated composites: mechanical and computational issues. International journal for numerical methods in engineering, 50(7):1701–1736, 2001.

[25] Milani, G., Lourenço, P. B., and Tralli, A.: Homogenised limit analysis of masonry walls, part i: Failure surfaces. Computers & structures, 84(3):166–180, 2006.

[26] Milani, G., Lourenço, P. B., and Tralli, A.: Homogenised limit analysis of masonry walls, part ii: Structural examples. Computers & structures, 84(3):181–195, 2006.

[27] Massart, T. J., Peerlings, R. H. J., and Geers, M. G. D.: An enhanced multi-scale approach for masonry wall computations with localization of damage. International Journal for Numerical Methods in Engineering, 69(5):1022–1059, 2007.

Appendix B (Continued)

[28] Sacco, E.: A nonlinear homogenization procedure for periodic masonry. European Journal of Mechanics-A/Solids, 28(2):209–222, 2009.

[29] Marfia, S. and Sacco, E.: Multiscale damage contact-friction model for periodic masonry walls. Computer Methods in Applied Mechanics and Engineering, 205:189–203, 2012.

[30] Chaimoon, K. and Attard, M. M.: Modeling of unreinforced masonry walls under shear and compression. Engineering structures, 29(9):2056–2068, 2007.

[31] Reyes, E., Casati, M., and Gálvez, J.: Cohesive crack model for mixed mode fracture of brick masonry. International Journal of Fracture, 151(1):29–55, 2008.

[32] Reyes, E., Gálvez, J., Casati, M., Cendón, D., Sancho, J., and Planas, J.: An embedded cohesive crack model for finite element analysis of brickwork masonry fracture. Engineering Fracture Mechanics, 76(12):1930 – 1944, 2009.

[33] Radulovic, R., Bruhns, O. T., and Mosler, J.: Effective 3d failure simulations by combining the advantages of embedded strong discontinuity approaches and classical interface elements. Engineering Fracture Mechanics, 78(12):2470–2485, 2011.

[34] Vandoren, B., De Proft, K., Simone, A., and Sluys, L. J.: Mesoscopic modelling of masonry using weak and strong discontinuities. Computer Methods in Applied Mechanics and Engineering, 255:167–182, 2013.

[35] Minaie, E., Moon, F. L., and Hamid, A. A.: Nonlinear finite element modeling of reinforced masonry shear walls for bidirectional loading response. Finite Elements in Analysis and Design, 84:44–53, 2014.

[36] Vyas, C. V. U. and Reddy, B. V.: Prediction of solid block masonry prism compressive strength using fe model. Materials and Structures, 43(5):719–735, 2010.

[37] Akbarzade M., A. and Tasnimi, A.: Nonlinear analysis and modeling of unreinforced masonry shear walls based on plastic damage model. Journal of Seismology and Earthquake Engineering, 11(4), 2010.

[38] Srisanthi, V., Keshav, L., Kumar, P. P., and Jayakumar, T.: Finite element and experimental analysis of 3d masonry compressed stabilised earth block and brick building models against earthquake forces. Civil Engineering, 2014.

[39] Bui, Q.-B. and Morel, J.-C.: Assessing the anisotropy of rammed earth. Construction and Building Materials, 23(9):3005 – 3011, 2009.

[40] Bui, Q.-B., Morel, J.-C., Hans, S., and Meunier, N.: Compression behaviour of non-industrial materials in civil engineering by three scale experiments: the case of rammed earth. Materials and structures, 42(8):1101–1116, 2009.

Appendix B (Continued)

[41] Silva, R., Oliveira, D., Schueremans, L., Lourenço, P., and Miranda, T.: Modelling the structural behaviour of rammed earth components. Proceedings of the Twelfth International Conference on Computational Structures Technology, 2014.

[42] Lorenzo Miccoli, Daniel V. Oliveira, R. A. S. U. M. L. S.: Static behaviour of rammed earth: experimental testing and finite element modelling. Materials and Structures, 2015.

[43] Ortiz, M., Leroy, Y., and Needleman, A.: A finite element method for localized failure analysis. Computer Methods in Applied Mechanics and Engineering, 61(2):189 – 214, 1987.

[44] Wells, G. and Sluys, L.: A new method for modelling cohesive cracks using finite elements. International Journal for Numerical Methods in Engineering, 50(12):2667–2682, 2001.

[45] Oliver, J., Cervera, M., and Manzoli, O.: Strong discontinuities and continuum plasticity models: the strong discontinuity approach. International Journal of Plasticity, 15(3):319 – 351, 1999.

[46] Belytschko, T. and Black, T.: Elastic crack growth in finite elements with minimal remeshing. International Journal of Num, 45:601–620, 1999.

[47] Moes, N., D. J. B. T.: A finite element method for crack growth without remeshing. International Journal for Num, 46(1):131–150, 1999.

[48] Sukumar, N., M. N. M. B. B. T.: Extended finite element method for three-dimensional crack modeling. International Journal of Numerical Methods in Engineering, 48:1549–1570, 2000.

[49] Dolbow, J., M. N. B. T.: Modeling fracture in mindlin-reissner plates with the extended finite element method. International Journal for Solids and Structures, 37:7161–7183, 2000.

[50] Babuska, I., S. T. C. K.: The design and analysis of the generalized finite element method. Computer Methods in, 181(1):43–69, 2000.

[51] Strouboulis, T., C. K. B. I.: The generalized finite element method: an example of its implementation and illustration of its performance. International Journal of Numerical Methods in Engineering, 47(8):1401–1417, 2000.

[52] Oliver, J., Huespe, A., Blanco, S., and Linero, D.: Stability and robustness issues in numerical modeling of material failure with the strong discontinuity approach. Computer Methods in Applied Mechanics and Engineering, 195(52):7093 – 7114, 2006. Computational Modelling of Concrete.

[53] Regueiro, R. A. and Borja, R. I.: A finite element model of localized deformation in frictional materials taking a strong discontinuity approach. Finite Elements in Analysis and Design, 33(4):283 – 315, 1999.

Appendix B (Continued)

[54] Regueiro, R. A. and Borja, R. I.: Plane strain finite element analysis of pressure sensitive plasticity with strong discontinuity. International Journal of Solids and Structures, 38(21):3647 – 3672, 2001.

[55] Borja, R. I. and Regueiro, R. A.: Strain localization in frictional materials exhibiting displacement jumps. Computer Methods in Applied Mechanics and Engineering, 190(2021):2555 – 2580, 2001.

[56] Borja, R. I. and Foster, C. D.: Continuum mathematical modeling of slip weakening in geological systems. Journal of Geophysical Research: Solid Earth, 112(B4):n/a–n/a, 2007.

[57] Foster, C. D., Borja, R. I., and Regueiro, R. A.: Embedded strong discontinuity finite elements for fractured geomaterials with variable friction. International Journal for Numerical Methods in Engineering, 72(5):549–581, 2007.

[58] Armero, F. and Garikipati, K.: An analysis of strong discontinuities in multiplicative finite strain plasticity and their relation with the numerical simulation of strain localization in solids. International Journal of Solids and Structures, 33(2022):2863 – 2885, 1996.

[59] Dugdale, D.: Yielding of steel sheets containing slits. Journal of the Mechanics and Physics of Solids, 8(2):100 – 104, 1960.

[60] Barenblatt, G.: The mathematical theory of equilibrium cracks in brittle fracture. Advances in Applied Mechanics, 7:55–129, 1962.

[61] Park, K. and Paulino, G.: Cohesive zone models: A critical review of traction-separation relationships across fracture surfaces. ASME. Applied Mechanics Review, 64(6), 2011.

[62] Weed, D. A., Foster, C. D., and Motamedi, M. H.: A combined opening-sliding formulation for use in modeling geomaterial deformation and fracture patterns. in review. Computers and Structures, 2015.

[63] Allix, O., Ladeveze, P., and Corigliano, A.: Damage analysis of interlaminar fracture specimens. Composite Structures, 31(1):61–74, 1995.

[64] Mroz, Z. and Giambanco, G.: An interface model for analysis of deformation behaviour of discontinuities. International journal for numerical and analytical methods in geomechanics, 20(1):1–33, 1996.

[65] Alfano, G. and Sacco, E.: Combining interface damage and friction in a cohesive-zone model. International Journal for Numerical Methods in Engineering, 68(5):542–582, 2006.

[66] Camanho, P. P. and Dávila, C. G.: Mixed-mode decohesion finite elements for the simulation of delamination in composite materials. NASA-Technical paper, 211737(1):33, 2002.

Appendix B (Continued)

[67] Camanho, P. P., Davila, C., and De Moura, M.: Numerical simulation of mixed-mode progressive delamination in composite materials. Journal of composite materials, 37(16):1415–1438, 2003.

[68] De Lorenzis, L.: Some recent results and open issues on interface modeling in civil engineering structures. Materials and structures, 45(4):477–503, 2012.

[69] Shieh-Beygi, B. and Pietruszczak, S.: Numerical analysis of structural masonry: mesoscale approach. Computers & Structures, 86(21):1958–1973, 2008.

[70] Belytschko, T., Fish, J., and Engelmann, B. E.: A finite element with embedded localization zones. Computer Methods in Applied Mechanics and Engineering, 70(1):59 – 89, 1988.

[71] Sluys, L. and Berends, A.: Discontinuous failure analysis for mode-i and mode-ii localization problems. International Journal of Solids and Structures, 35(3132):4257 – 4274, 1998.

[72] Tresca, M. H.: On further applications of the flow of solids. Journal of the Franklin Institute, 106(5):326 – 334, 1878.

[73] Simo, J. C. and Rifai, M. S.: A class of mixed assumed strain methods and the method of incompatible modes. International Journal for Numerical Methods in Engineering, 29(8):1595–1638, 1990.

[74] Daneshyar, A. and Mohammadi, S.: Strong tangential discontinuity modeling of shear bands using the extended finite element method. Computational Mechanics, 52(5):1023–1038, 2013.

[75] Carol, I., Prat, P., and Lpez, C.: Normal/shear cracking model: Application to discrete crack analysis. Journal of Engineering Mechanics, 123(8):765–773, 1997.

[76] Camacho, G. and Ortiz, M.: Computational modelling of impact damage in brittle materials. International Journal of Solids and Structures, 33(2022):2899 – 2938, 1996.

[77] Truster, T. and Masud, A.: A discontinuous/continuous galerkin method for modeling of interphase damage in fibrous composite systems. Computational Mechanics, 52(3):499–514, 2013.

[78] Wang, Y. and Waisman, H.: Progressive delamination analysis of composite materials using xfem and a discrete damage zone model. Computational Mechanics, 55(1):1–26, 2015.

[79] Mosler, J. and Meschke, G.: 3d modelling of strong discontinuities in elastoplastic solids: fixed and rotating localization formulations. International Journal for Numerical Methods in Engineering, 57(11):1553–1576, 2003.

Appendix B (Continued)

[80] Dieterich, J. H. and Linker, M. F.: Fault stability under conditions of variable normal stress. Geophysical Research Letters, 19(16):1691–1694, 1992.

[81] Jirásek, M.: Comparative study on finite elements with embedded discontinuities. Computer Methods in Applied Mechanics and Engineering, 188(13):307 – 330, 2000.

[82] Borja, R. I.: A finite element model for strain localization analysis of strongly discontinuous fields based on standard galerkin approximation. Computer Methods in Applied Mechanics and Engineering, 190(11):1529–1549, 2000.

[83] Hill, R.: Acceleration waves in solids. Journal of the Mechanics and Physics of Solids, 10(1):1 – 16, 1962.

[84] Rudnicki, J. and Rice, J.: Conditions for the localization of deformation in pressure-sensitive dilatant materials. Journal of the Mechanics and Physics of Solids, 23(6):371 – 394, 1975.

[85] Wells, G. and Sluys, L.: Application of embedded discontinuities for softening solids. Engineering Fracture Mechanics, 65(23):263 – 281, 2000.

[86] Oliver, J.: On the discrete constitutive models induced by strong discontinuity kinematics and continuum constitutive equations. International Journal of Solids and Structures, 37(4850):7207 – 7229, 2000.

[87] Alfaiate, J., Wells, G., and Sluys, L.: On the use of embedded discontinuity elements with crack path continuity for mode-i and mixed-mode fracture. Engineering Fracture Mechanics, 69(6):661 – 686, 2002.

[88] Yin, A., Yang, X., Gao, H., and Zhu, H.: Tensile fracture simulation of random heterogeneous asphalt mixture with cohesive crack model. Engineering Fracture Mechanics, 92(0):40 – 55, 2012.

[89] Ayatollahi, M. and Sistaninia, M.: Mode ii fracture study of rocks using brazilian disk specimens. International Journal of Rock Mechanics and Mining Sciences, 48(5):819 – 826, 2011.

[90] Motamedi, M. and Foster, C. D.: An improved implicit numerical integration of a non-associated, three-invariant cap plasticity model with mixed isotropickinematic hardening for geomaterials. International Journal For Numerical and Analytical Methods in Geomechanics, 2015.

[91] Mair, K. and Abe, S.: Breaking up: Comminution mechanisms in sheared simulated fault gouge. Pure and Applied Geophysics, 168(12):2277–2288, 2011.

[92] Hillerborg, A., Modéer, M., and Petersson, P.-E.: Analysis of crack formation and crack growth in concrete by means of fracture mechanics and finite elements. Cement and Concrete Research, 6(6):773 – 781, 1976.

Appendix B (Continued)

[93] Guinea, G., Planas, J., and Elices, M.: A general bilinear fit for the softening curve of concrete. Materials and Structures, 27(2):99–105, 1994.

[94] Yang, Z. and Xu, X. F.: A heterogeneous cohesive model for quasi-brittle materials considering spatially varying random fracture properties. Computer Methods in Applied Mechanics and Engineering, 197(4548):4027 – 4039, 2008.

[95] Cornelissen, H., Hordijk, D., and Reinhardt, H.: Experimental determination of crack softening characteristics of normalweight and lightweight concrete. Heron, 31(2):45–56, 1986.

[96] Wu, J.-Y., Li, F.-B., and Xu, S.-L.: Extended embedded finite elements with continuous displacement jumps for the modeling of localized failure in solids. Computer Methods in Applied Mechanics and Engineering, 285:346 – 378, 2015.

[97] Reinhardt, H.: Fracture mechanics of fictitious crack propagation in concrete. Heron, 29(2):3–42, 1984.

[98] Ida, Y.: Cohesive force across the tip of a longitudinal-shear crack and griffith's specific surface energy. Journal of Geophysical Research, 77(20):3796–3805, 1972.

[99] Rinehart, A. J., Bishop, J. E., and Dewers, T.: Fracture propagation in indiana limestone interpreted via linear softening cohesive fracture model. Journal of Geophysical Research: Solid Earth, 120(4):2292–2308, 2015. 2014JB011624.

[100] Jirásek, M. and Belytschko, T.: Computational resolution of strong discontinuities. In Proceedings of Fifth World Congress on Computational Mechanics, WCCM V, Vienna University of Technology, Austria, 2002.

[101] Regueiro, R. A. and Foster, C. D.: Bifurcation analysis for a rate-sensitive, non-associative, three-invariant, isotropic/kinematic hardening cap plasticity model for geomaterials: Part i. small strain. International Journal for Numerical and Analytical Methods in Geomechanics, 35(2):201–225, 2011.

[102] Gens, A., Carol, I., and Alonso, E.: An interface element formulation for the analysis of soil-reinforcement interaction. Computers and Geotechnics, 7(12):133 – 151, 1989. Special Issue on Soil Reinforcement.

[103] de Borst, R. and Remmers, J. J.: Computational modelling of delamination. Composites Science and Technology, 66(6):713 – 722, 2006. Advances in statics and dynamics of delaminationWorkshop on Advances in Modeling Delamination in Composite Materials and Structures.

[104] Schellekens, J. and De Borst, R.: On the numerical integration of interface elements. International Journal for Numerical Methods in Engineering, 36:43–66, 1993.

Appendix B (Continued)

[105] Lourenco, P. B., Rots, J. G., and Blaauwendraad, J.: Continuum model for masonry: Parameter estimation and validation. Journal of Structural Engineering, 124(6):642–652, 1998.

[106] Ericson, C.: Real-Time Collision Detection (The Morgan Kaufmann Series in Interactive 3-D Technology). CRC Press, 2004.

[107] Tennant, A. G., M. R. B. V. P. F. C. P.: Detailed experimental review of flexural behavior of cement stabilized soil block masonry (pending approval). Journal of Materials in Civil Engineering, 2015.

[108] Chaimoon, K. and Attard, M. M.: Experimental and numerical investigation of masonry under three-point bending (in-plane). Engineering Structures, 31(1):103–112, 2009.

[109] Reddy, B. V. V., Lal, R., and Rao, K. S. N.: Enhancing bond strength and characteristics of soil-cement block masonry. Journal of Materials in Civil Engineering, 19(2):164–172, February 2007 2007.

[110] Reddy, B. V. V. and Latha, M. S.: Influence of soil grading on the characteristics of cement stabilised soil compacts. Materials and Structures, 47(10):1633 – 1645, 2013.

[111] Jayasinghe, C. and Kamaladasa, N.: Compressive strength characteristics of cement stabilized rammed earth walls. Construction and Building Materials, 21(11):1971 – 1976, 2007.

[112] Lombillo, I., Villegas, L., Fodde, E., and Thomas, C.: In situ mechanical investigation of rammed earth: Calibration of minor destructive testing. Construction and Building Materials, 51:451 – 460, 2014.

[113] Tennant, A. G., Foster, C. D., and Reddy, B. V.: Verification of masonry building code to flexural behavior of cement-stabilized soil block. Journal of Materials in Civil Engineering, 25(3):303–307, 2012.

[114] Oliver, J. and Huespe, A.: Continuum approach to material failure in strong discontinuity settings. Computer Methods in Applied Mechanics and Engineering, 193(3032):3195 – 3220, 2004. Computational Failure Mechanics.

[115] Motamedi, M. H., F. C. W. D.: Numerical simulation of mixed mode (i and ii) fracture behavior of pre-cracked rock using the strong discontinuity approach. International Journal of Solids, In review.

[116] Foster, C., Regueiro, R., Fossum, A., and Borja, R.: Implicit numerical integration of a three-invariant, isotropic/kinematic hardening cap plasticity model for geomaterials. Computer Methods in Applied Mechanics and Engineering, 194(50-52):5109–5138, December 2005.

[117] Fossum, A. F. and Brannon, R. M.: The Sandia GeoModel: theory and user's guide. SAND report August, Sandia National Laboratories, 2004.

[118] Sun, W., Chen, Q., and Ostien, J. T.: Modeling the hydro-mechanical responses of strip and circular punch loadings on water-saturated collapsible geomaterials. Acta Geotechnica, 9(5):903–934, 2014.

[119] Gudehus, G.: Elastoplastische stoffgleichungen fr trockenen sand. Ingenieur-Archiv, 42(3):151–169, 1973.

[120] Armero, F. and Kim, J.: Three-dimensional finite elements with embedded strong discontinuities to model material failure in the infinitesimal range. International Journal for Numerical Methods in Engineering, 91(12):1291–1330, 2012.

[121] Linder, C. and Armero, F.: Finite elements with embedded strong discontinuities for the modeling of failure in solids. International Journal for Numerical Methods in Engineering, 72(12):1391–1433, 2007.

VITA

David A. Weed

945 West 32nd Street

Chicago, IL 60608

(708) 705-9091

david.weed@gmail.com

OBJECTIVE

Computational mechanics scientist seeking to utilize my expertise with designing numerical algorithms and modeling biological tissues and geomaterials via the finite element method in either a research or industry-related position.

EDUCATION

Bachelor of Engineering, Bioengineering May 2006

Minor, Mechanical Engineering

University of Illinois at Chicago, Chicago, IL

Associate of Science May 2002

Prairie State College, Chicago Heights, IL

TECHNOLOGY/SKILLS

Programming Languages: Python, Java, C++.

Software: Matlab, Ansys, Abaqus, Microsoft Office Suite.

EXPERIENCE

Graduate Research Assistant January 2009 - December 2015

Department of Civil and Materials Engineering

University of Illinois at Chicago, IL 60607

- PhD dissertation focus on numerical modeling of solid structures using enhanced finite element techniques designed to capture inelastic and fracture behavior of geological materials and earthen-based structures.
- Collaborated with researchers at IISc (Indian Institute of Science in Bangalore, India) who provided empirical data from physical experiments used to verify numerical model for simulating behavior of cement soil stabilized block (CSSB) masonry.
- Performed parameterization on experimental data to find parameters for theoretical plasticity and fracture constitutive models.

- Formulated and implemented a novel constitutive model which tracks fracture damage throughout structures composed of earthen-based brick and mortar.
- Designed and implemented software algorithms to enhance the numerical robustness of finite element simulations (e.g., an implicit-explicit solver that leads to robust convergence).
- Successfully predicted flexure and peak load of masonry wall specimens through finite element simulations.

Graduate Research Assistant September 2006 - August 2008

Department of Mechanical Engineering

University of Illinois at Chicago, IL 60607

- Simulated multi-body systems using finite element simulation software.
- Authored subroutines in Fortran to implement novel joint constraints in multi-body systems.
- Developed an anatomical knee model with implementation of Neo-Hookean constitutive model for simulating motion and behavior of knee ligaments.

Undergraduate Research Assistant October 2003 - May 2005

Department of Civil and Materials Engineering

University of Illinois at Chicago, IL 60607

- Prepared fiber optic connectors for the interferometry system used in sensing strain during compression tests of concrete.
- Prepared and mixed several batches of concrete specimens (cylinders, beams, and cubes).
- Performed compression tests on concrete samples analyzing strength and shear modulus.
- Performed fresh paste rheological tests.
- Carried out data acquisition and processing using data acquisition system.

JOURNAL PUBLICATIONS

- B. Hussein, **D.A. Weed**. *Clamped End Conditions and Cross Section Deformation in the Finite Element Absolute Nodal Coordinate Formulation.* Journal of Multibody System Dynamics Vol. 21 (4), pp. 375-393, 2009.
- **D.A. Weed**, L.G. Maqueda, M.A. Brown, A.A. Shabana. *A New Nonlinear Multibody/Finite Element Formulation for Knee Joint Ligaments.* Journal of Nonlinear Dynamnics, 2009.
- **D.A. Weed**, C.D. Foster and M.H. Motamedi. *A Combined Opening-Sliding Formulation for use in Modeling Geomaterial Deformation and Fracture Patterns.* Under review.
- M.H. Motamedi, **D.A. Weed** and C.D. Foster. *Numerical Simulation of Mixed-Mode (I and II) Fracture Behavior of Pre-cracked Rock Using the Strong Discontinuity Approach.* Accepted.

PAPERS IN PREPARATION

- **D.A. Weed**, A.G. Tennant, M.H. Motamedi, C.D. Foster and B.V. Reddy. *Finite Element Model Application to Flexural Behavior of Cement Stabilized Soil Block Masonry.*
- **D.A. Weed** and C. D. Foster. *A New Method for Embedding Pre-existing Interfaces in Geomaterials.*

CONFERENCE PRESENTATIONS

- **D.A. Weed**, L.G. Maqueda, M.A. Brown, A.A. Shabana. *A Multibody/Finite Element Non-linear Formulation of a Two-ligament Knee Joint.* ASME National Congress, Boston, 2008
- C.D. Foster and **D.A. Weed**. *Fracture and Failure Modeling in Earthen Structural Materials.* International Conference on Computational Modeling of Fracture and Failure of Materials and Structures (CFRAC 2011), Barcelona, Spain.
- **D.A. Weed**, C.D. Foster. *Modeling Deformation and Failure in Earthen Structural Materials.* 11th U.S. National Congress on Computational Mechanics, 2011, Minneapolis, Minnesota.
- **D.A. Weed**, C.D. Foster. *Capturing Fracture Modes in Soil-Based Materials Using Enhanced Finite Elements.* 12th U.S.National Congress on Computational Mechanics, 2013, Raleigh, North Carolina.

- **D.A. Weed**, A.G. Tennant, C.D. Foster. *Cement Stabilized Earth Block Wall Experimentation and Computational Modeling.* 2013 Conference of the ASCE Engineering Mechanics Institute, Evanston, Illinois.

COURSES TAKEN

Introductory Finite Element Analysis, Advanced Finite Element Analysis, Plasticity Theory, Continuum Mechanics, Computational Continuum Mechanics, Numerical Methods in Engineering, Computer Aided Analysis of Multibody Systems I and II, Statistics, Biomechanics, Biomechanics of the Human, Computational Biomechanics, Human Anatomy and Physiology, Medical Product Development, Bioinstrumentation I and II.

TEACHING/TUTORING EXPERIENCE

Intermediate Algebra, College Algebra, Pre-Calculus, Calculus 1, 2 and 3 (Fall 2000 Spring 2002), Engineering Statics (Fall 2009), Strength of Materials/Mechanics of Materials (Fall 2010), Introductory Finite Element Analysis (Fall 2008, Fall 2013), Properties of Materials (Spring 2015).

GENERAL INTERESTS

Teaching/Mentoring, Numerical algorithm design, Finite element analysis, Geomechanics, and Biomechanics.

AWARDS/RECOGNITION/FELLOWSHIPS

- Bridge to the Doctorate Fellow (2006)
- Won first place at 2005 UIC Engineering Expo for Senior Design project
- NACME Scholar (2003)

LinkedIn Address: https://www.linkedin.com/in/davidaweed